FACULTY OF INFORMATION TECHNOLOGY AND ELECTRICAL ENGINEERING
DEGREE PROGRAMME IN ELECTRONICS AND COMMUNICATIONS ENGINEERING

MASTER'S THESIS

Characterization of electromagnetic absorption materials with two distinct methods

Author	Niklas Ilonen
Supervisor	Jarkko Tolvanen
Second Examiner	Mikko Nelo

June 2022

Ilonen N. (2022) Characterization of electromagnetic absorption materials with two distinct methods. University of Oulu, Faculty of Information Technology and Electrical Engineering, Degree Programme in Electronics and Communications Engineering, Master's Thesis, 57 p.

ABSTRACT

In this work, the task was to characterize the electromagnetic absorbers, made of multi-layered composite materials, and then to compare the measurement results of two different methods.

In total, seven different composites were made by using polyurethane as a matrix, hollow glass and fly ash microspheres, combination of blast furnace and steel smelter dusts, and carbon nanotubes as fillers. The purpose was to prepare multi-layered absorbers with resistive and magnetic gradient to achieve a good attenuation characteristic at microwave frequencies.

The work was split into two parts. In first part, a MATLAB code was written for the measurements. On the second part, the prepared anisotropic and multi-layered absorbers were characterized by two different measurements setups. The characterization was done with a two-port waveguide measurement and a one-port measurement with dielectric assessment kit (DAK-TL) at 18-26.5 GHz and 4-20 GHz frequency ranges, respectively.

In this work, microwave attenuation characteristics, such as shielding effectiveness values and reflection loss were measured. The comparison was done to determinate the reliability of the methods to characterize the absorbers.

Key words: electromagnetic interference shielding, measurement methods, radiant-absorber material, absorption materials, shielding effectiveness.

Ilonen N. (2022) Sähkömagneettisten absorptiomateriaalien karakterisointia kahdella erillisellä menetelmällä. Oulun yliopisto, tieto- ja sähkötekniikan tiedekunta, elektroniikan ja tietoliikennetekniikan tutkinto-ohjelma. Diplomityö, 57 s.

TIIVISTELMÄ

Tässä työssä tehtävänä oli karakterisoida sähkömagneettisia vaimennusmateriaaleja, jotka valmistettiin monikerroksisista komposiittimateriaaleista, jonka jälkeen vertailtiin kahden eri menetelmän mittaustuloksia.

Yhteensä tehtiin seitsemän erilaista komposiittia käyttämällä polyuretaania matriisina, onttoja lasi- ja lentotuhkamikropalloja, masuunin ja terässulaton pölyjä sekä hiilinanoputkia täyteaineena. Tarkoituksena oli valmistaa monikerrosrakenteita, joissa on resistiivinen ja magneettinen gradientti, jotta saataisiin hyvät vaimennusominaisuudet mikroaaltotaajuuksilla.

Työ jaettiin kahteen osaan. Ensimmäisessä osassa kehitettiin MATLAB-koodi mittauksia varten. Toisessa osassa valmistettuja anisotrooppisia ja monikerroksellisia vaimennusmateriaaleja karakterisoitiin kahdella eri mittausmenetelmällä. Karakterisointi tehtiin kaksiporttisella aaltoputkimittauksella ja yksiporttisella mittapäällä (DAK-TL) taajuusalueilla 18-26.5 GHz ja 4-20 GHz.

Työssä mitattiin mikroaaltovaimennusominaisuuksia, kuten suojauksen tehokkuusarvoja ja heijastushäviöitä. Vertailu tehtiin vaimennusmateriaalien karakterisointimenetelmien luotettavuuden määrittämiseksi.

Avainsanat: sähkömagneettinen häiriösuojaus, mittausmenetelmät, säteilyn vaimennusmateriaali, vaimennusmateriaali, suojaustehokkuus.

TABLE OF CONTENTS

FOREWORD

This thesis work was carried out at the University of Oulu in Microelectronics Research Unit for the completion of my master's degree.

I am grateful to my supervisors Jarkko Tolvanen and Mikko Nelo for supervising this thesis. Their constant support, comments, and reviews were extremely crucial for the completion of the Master thesis. I would also like especially to thanks Jarkko Tolvanen for assisting me during the measurements in the laboratory and looking into all technical aspects of the thesis.

I want also to thank my parents and my brother for the support and encouraging me though every step of this arduous journey.

Oulu, June 30, 2022

Niklas Ilonen

LIST OF ABBREVIATIONS AND SYMBOLS

CB	carbon black
CNT	carbon nanotubes
DAK-TL	dielectric assessment kit for thin layers
EM	electromagnetic
HGMS	hollow glass microspheres
NIST	non-iterative stable transmission
RL	reflection loss
SCL	short circuit line
TE	transverse electric
TEM	transverse electromagnetic
TL	transmission line
TM	transverse magnetic
VNA	vector network analyzer
5G	fifth-generation network
A	absorption coefficient
a	length of waveguide
b	length of waveguide
B	effective impedance
c	speed of light
t	thickness
e	Euler's number
E_1	inside shield transmitted electric wave
E_i	incident wave in electric field
E_t	transmitted wave in electric field
E_r	reflected wave in electric field
f	frequency
f_c	cut-off frequency
H_1	inside shield transmitted magnetic wave
H_i	incident wave in magnetic field
H_r	reflected wave in magnetic field
H_t	transmitted wave in magnetic field
$\overrightarrow{J_{ms}}$	magnetic surface current source
$\overrightarrow{J_s}$	surface current source
L	distance from short circuit to sample
l	length
m	number of half cycle variations of the fields in the x-direction
n	number of half cycle variations of the fields in the y-direction
n_{int}	integer determined from group delay
p	position at the frequency
Q	phase
SE_A	shielding effectiveness for absorption
SE_M	shielding effectiveness for multiple reflections
SE_R	shielding effectiveness for reflections
SE_T	total shielding effectiveness
S_{11}	scattering parameter for reflection coefficient

S_{22}	scattering parameter for reflection coefficient
S_{12}	scattering parameter for transmission coefficient
S_{21}	scattering parameter for transmission coefficient
Z_S	normalized surface impedance
T	transmission coefficient
$tan(\delta)$	tangent loss
$tan(\delta_\varepsilon)$	dielectric loss tangent factor
$tan(\delta_\mu)$	magnetic loss tangent factor

α	attenuation constant
β	phase constant
γ	propagation constant
γ_0	propagation constant of free space
Γ or R	reflection coefficient
δ	skin depth
δ''	divided part in loss tangent
δ'	divider part in loss tangent
ε	permittivity
ε_0	permittivity of free space
ε'	real part of relative permittivity
ε''	imaginary part of relative permittivity
η	characteristic impedance
η_0	characteristic impedance of free space
η_{in}	characteristic input impedance
Λ	loaded guided waveguide
λ_c	cut-off wavelength
λ_0	free space wavelength
λ_{0g}	empty guided wavelength
μ	permeability
μ_0	permeability of free space
μ'	real part of relative permeability
μ''	imaginary part of relative permeability
ρ	resistivity
σ	conductivity
ω	angular frequency

1 INTRODUCTION

Absorber materials are material structures that absorb incoming electromagnetic (EM) waves by mutually cancelling the phases and converting the energy into heat, so that no surface reflection occurs. [1] The ideal absorbers would be thin, light, inexpensive, long lasting and have broadband coverage of frequency [2]. The concept of EM wave absorber is that a structure has an ability to absorb incoming incident EM waves and turn them on the impact of the surface.

Shielding refers to materials that may block or reduce the EM wave propagation to product or from the product [3,4]. This way the propagation of EM fields from one region to another can be controlled [4]. There are two primary purposes to shield electronic products. The first is to prevent any kind of emissions from the electronics to outside of the boundaries of the product [3]. Hence, prevent emissions causing the product to fail to comply with the radiated emissions limits or to prevent the product from causing any interference with other electrical devices [3]. The other reason for shielding is to prevent, for example, EM waves reaching an isolated product inside the shielded area [3].

The shielding effectiveness of a shield can be viewed as a ratio of the magnitude of the electric and magnetic field that is incident on the barrier to the magnitude of the electric and magnetic field which transmit through the barrier. [3]

The important properties of absorption materials are the electromagnetic wave attenuation characteristics that relate to the magnetic and dielectric properties of the material. It is necessary to understand that how the electric and magnetic waves interact with the material [5]. This interaction between EM waves and material depends on the frequency and the filler particles inside an absorber or a shielding material [5]. Due operation frequency becoming higher and the number of electronic devices increasing, wireless communication and fifth-generation networks (5G) becoming more present, it is necessary to provide shielding as these may have impact on devices [6]. As a result, the engineers constantly try to find new innovative ways to improve already existing absorption materials and structures, while also trying to develop new ones.

Another aspect related to absorption materials is that how the attenuation characteristics are measured. There is wide variety of different methods available, because it is important to have accurate and reliable measurements. Properties such as a permittivity, a permeability, and a conductivity [7] are usually focus of the measurement methods because it is possible to define absorption materials properties as mentioned before. For this reason, two methods were chosen and compared: Nicolson-Ross-Weir and Short circuit line iteration method.

The objective of this work was to characterize the electromagnetic absorbers made of multi-layered composite materials, and then to compare the measurement results of two different methods made with waveguide and DAK-TL. For the purpose, three-layered anisotropic composite materials were made by incorporation electric and magnetic fillers to polyurethane for controlling the impedance and attenuation characteristics at the microwave frequencies. Furthermore, the work gives a comprehensive theoretical background to the absorber and electromagnetic interference shielding properties, for example, on the basis of transmission line theory, Weston's theorem and Maxwell's equations.

2 ABSORBTION MATERIAL STRUCTURES AND PROPERTIES

2.1 Materials

There exist three basic electromagnetic absorber structures, which can be either single- or multi-layered material structures made with conductive, dielectric and/or magnetic fillers [1,8].

The resistive-type absorber materials absorb the electromagnetic (EM) waves, and the magnitude of the absorption depends on the conductance and permittivity of the material. Resistive-type absorbers are usually composite materials which typically use electric fillers, such as carbon black (CB), graphene, carbon nanotubes, or even metallic powders and silicon carbide. [8]

The dielectric absorber materials consist, for example, of carbon rubber, urethane foam and expanded polystyrene. Dielectric absorber materials can be used to realize broadband absorption characteristics and applied into multilayered structures. [1] Idea of the dielectric absorber materials is to control the impedance and dielectric loss characteristics. The EM waves are absorbed by dielectric absorbers through the dielectric relaxation processes [8].

Absorption of EM waves is strongly controlled by the frequency dispersion characteristic of magnetic materials which on contrast is controlled by a permeability. As for the magnetic fillers, for example, ferrites, carbonyl iron and other like materials that are magnetically lossy, and these materials can be made into films, sheets, or coatings. [1]

For good absorber performance an important requirement is that they have low reflection and achieve a good attenuation of EM waves. With new materials and structures, the absorbers may become yet more thinner, have wider absorption bandwidth, and improved mechanical properties. [8]

2.2 Structures

Conventional structures for electromagnetic absorbers are Salisbury screen, Jaumann and Dallenbach absorbers. Salisbury screen is a resonant absorber which relays on the relative permittivity and permeability value to control the impedance. The Salisbury screen consist mainly of two layers. The first layer is often resistive sheet, with matched level of conductance, that is placed from ¼ wavelength of a metallic surface with a large surface reflectivity. These layers can be either separated by an air gap or a material with a specific value of relative permittivity can replace the air gap. The addition of dielectric can decrease the required distance between the resistive sheet and metallic surface at the expense of bandwidth. [9–11]

The Jaumann absorber increases the bandwidth of a Salisbury screen by adding an additional resistive sheet(s) and spacer(s) [2]. Although, the basic principle is still the same (¼ wavelength distance between all layers). In multi-layer Jaumann absorber low loss dielectric sheets are separating the individual resistive sheets. The idea is to have a resistive gradient within the structure, where resistivity of the sheets decreases towards a metallic plate [9].

The Dallenbach absorber is probably one of the simplest designs as it is composed of two layers [2]. The first layer consists of the absorbing layer (a homogenous lossy coating layer) [2,9], which then can consist of multiple individual layers that are placed layer after layer. Absorber layer structure is followed by a metallic plate [2].

The reflection of EM waves from a surface at the air-media interface is due to impedance mismatch. Therefore, it is important to find a material whose impedance relative to

free space is equal to 1 at wide frequency band. [2] This allows minimizing the reflectivity for the desired frequency range and achieving an efficient wide-band absorption of EM waves with good attenuation (assuming the material is lossy).

Dallenbach layer absorber is shown in Figure 1. The incident EM wave propagates into a homogenous layered absorber. Figure 1b shows more precisely how the incident EM wave gets reflected and transmitted inside absorber. The absorber consists of multiple different layers with variable permittivity and permeability values and thicknesses of individual layers. The incident EM wave gets reflected inside the absorber at the material interfaces, while some these waves are absorbed and then further converted and dissipated as heat.

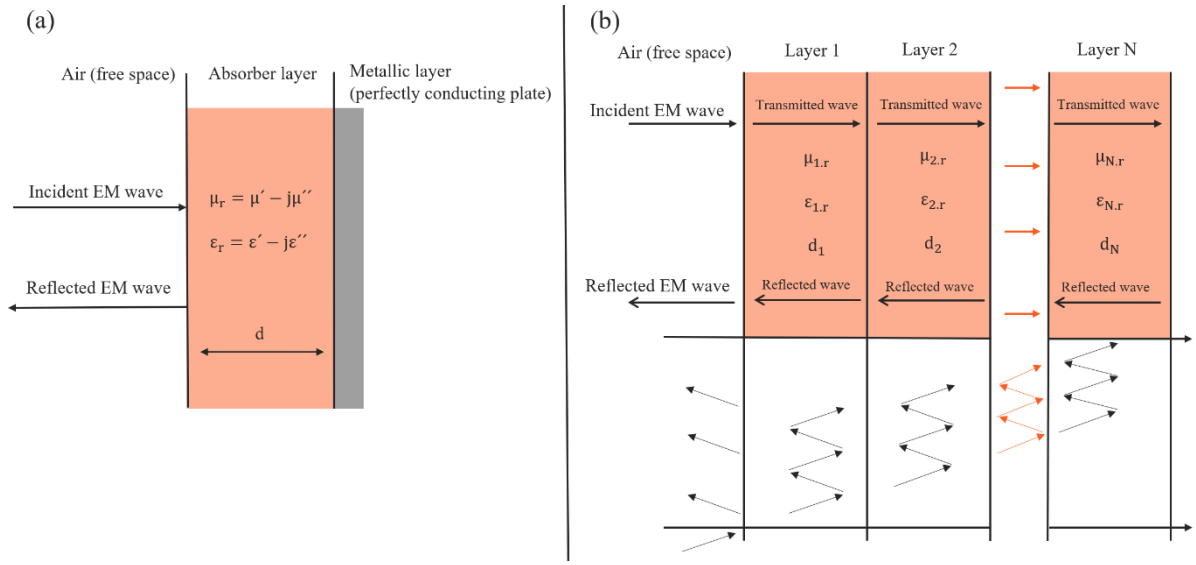

Figure 1. Illustration of (a) Dallenbach layer and (b) multi-layered absorber with variable refractive index, and propagation of EM waves propagate inside the layers.

2.3 Material properties

Several material properties affect the overall performance of electromagnetic absorber. In this section, dielectric and magnetic properties, dielectric loss mechanisms, and skin depth will be covered. Each of these frequency-dependent properties has its own purpose in for performance characteristics of the absorbing materials.

2.3.1 Dielectric and Magnetic properties

Complex relative permittivity (ε_r) and complex relative permeability (μ_r) are important parameters because they determinate the reflection and attenuation characteristics of the absorbing materials [12–15]. Equations (1-2) [12,13,15] show the complex relatives:

$$\mu_r = \mu' - j\mu'', \quad (1)$$

$$\varepsilon_r = \varepsilon' - j\varepsilon'', \quad (2)$$

where μ' and μ'' are a real and an imaginary part of relative permeability, respectively, while the ε' and ε'' are a real and an imaginary relative permittivity, respectively.

The relative permeability and permittivity can be also written as in equations (3-4):

$$\mu_r = \frac{\mu}{\mu_0}, \tag{3}$$

$$\varepsilon_r = \frac{\varepsilon}{\varepsilon_0}, \tag{4}$$

where μ_0 and ε_0 are a permeability and a permittivity of free space. The equations (3-4) can be used for computing the relative permeability and permittivity with the knowledge of μ and ε for a material.

In complex formats, the real and imaginary parts of the relative permittivity and permeability represent different properties. The real parts ε' and μ' represent how well the material can store the electrical and magnetic energies, while the imaginary parts of the ε'' and μ'' represent the loss capabilities of the electric and magnetic energy [12,13,15] (Figure 2). The term loss itself may refer to the dissipation of power or energy quite analogous to the way energy is consumed by a resistor when an electric current passes through it [16]. Through losses electric or magnetic energy can be converted into heat. [16]

It is possible to obtain the magnetic and dielectric loss tangents from the real and imaginary values of complex relative permeability and permittivity by using the equations (5-6) [13,17]. The magnetic and dielectric loss tangents mean how much energy is lost in relation to the stored energy due to the magnetic or electric field, respectively.

$$tan(\delta_\mu) = \frac{\mu''}{\mu'}, \tag{5}$$

$$tan(\delta_\varepsilon) = \frac{\varepsilon''}{\varepsilon'}, \tag{6}$$

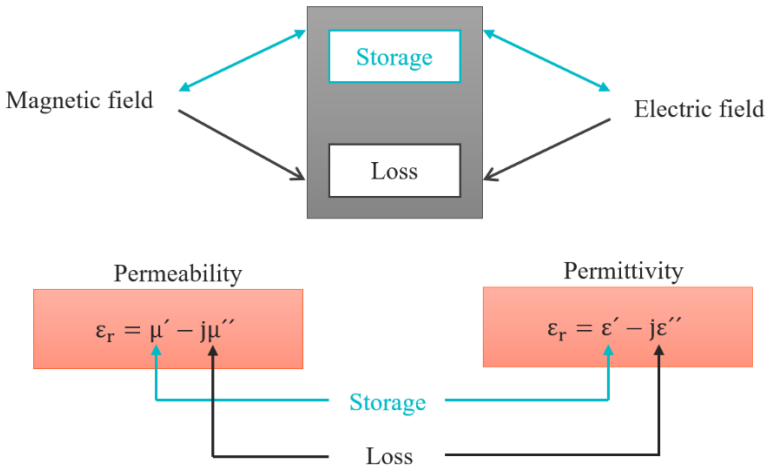

Figure 2. The real parts do work as (storages) for electric and magnetic waves energies, while imaginary parts work as dissipation (losses) for electric and magnetic waves energies.

2.3.2 Dielectric loss mechanisms

Dielectric relaxation processes are often a main cause of EM wave dissipation in electromagnetic absorbers. Dielectric losses can be retained even at high temperatures which makes them superior in that regard to magnetic lossy materials. In this section the main mechanisms will be briefly discussed for dielectric lossy materials, such as interfacial polarization, dipolar polarization, defect-induced polarization, and conductive loss. [18]

Interfacial polarization can be referred as Maxwell Wagner Sillars (MWS) effect. The interfacial polarization is stronger for heterogenous than for homogenous interfaces, can be present in porous/hollow structures. The positive and negative charged particles inside the material cause the interfacial polarization at heterogenous interfaces. [18]

Dipolar polarization is related to movements of dipoles in polar and nonpolar molecules that under effects of electromagnetic field. In non-polar molecules, the dipoles are generated by displacement of positive and negative charged molecular chains, which is called as a displacement polarization. If the polar molecules are rearranged, this leads to orientation polarization. [18]

Defect induced polarization is associated with defect sites that are areas where charged carriers are trapped, thus balance of charged carriers distribution is uneven. This kind distribution leads to polarization and EM energy losses. [18]

Another dielectric loss mechanisms is a conductive loss. The conductive loss is caused by EM wave propagation in an absorber when EM energy is converted into an electric current. During the transmission of electric current along the absorber, this will generate a joule heat, which will consume the EM wave energy. Conductive loss requires a high conductivity, but this may results into impedance mismatch and high surface reflection. [18]

2.3.3 Skin depth

The skin depth (δ) is the distance required of electromagnetic waves to travel inside the material to decay to 1/e (37 %) of its value (Figure 3) [19]. The δ is a frequency-dependent property often used for good conductors [20]. When a frequency increases, the value of δ becomes smaller. Current often concentrates near the surface of the conductor and decreases deeper inside of the skin of conductor [21]. The skin depth does not just depend on the frequency but also strongly related to materials resistivity [20,21].

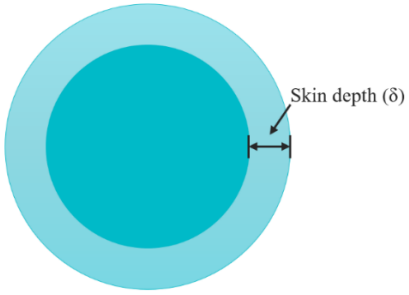

Figure 3. Skin depth is the depth from the edge of conductor to certain point where the current density has attenuated to value 1/e.

The skin depth can be expressed on the basis of equations (7-8):

$$\omega = 2\pi f, \tag{7}$$

$$\rho = \frac{1}{\sigma} \rightarrow \sigma = \frac{1}{\rho}, \tag{8}$$

where f is a frequency and ρ is resistivity of a material.

The skin depth can be expressed as seen in the equations (9-10) [20,21]:

$$\delta = \sqrt{\frac{2\rho}{\omega\mu}} \rightarrow = \sqrt{\frac{2\rho}{\omega\mu_r\mu_0}}, \tag{9}$$

$$\delta = \sqrt{\frac{2\frac{1}{\sigma}}{\omega\mu_r\mu_0}} = \sqrt{\frac{2\frac{1}{\sigma}}{2\pi f\mu_r\mu_0}} = \sqrt{\frac{\frac{1}{\sigma}}{\pi f\mu_r\mu_0}} = \frac{1}{\sqrt{\pi f\sigma\mu_r\mu_0}}, \tag{10}$$

where μ is a permeability that can be solved from the equation (3) by using the permittivity and permeability values of a free space. In the equation (9), the permeability for the free space equals to $4\pi \cdot 10^{-7}$ H m^{-1}.

The equation (10) can be further reduced to the equation (11) [22]:

$$\delta = \frac{1}{\alpha} = \alpha^{-1} = \frac{1}{\sqrt{\pi f\sigma\mu_r\mu_0}}, \tag{11}$$

where α is an attenuation constant (which is a real part of propagation constant γ).

2.3.4 Impedance (Weston´s theorem)

In the case of absorbers constructed of multiple discrete layers, the impedance can be explained by using the Weston´s theorem. First, it is important to understand how plane waves scatter at the material interfaces, and how dielectric and magnetic properties relate to the attenuation characteristics. V.H. Weston originally developed two important theorems that were derived from the Maxwells equations and the boundary conditions [16,23]. These conditions apply to all frequencies and include the possible scattering and loss mechanisms [16,23].

In the first Weston's theorem, it was stated that if an EM wave is incident to a body composed of material (where $\mu/\mu_0 = \varepsilon/\varepsilon_0$), the relative permittivity and relative permeability are equal at every point and invariant even under 90-degree rotation of the axis of the body. Thus, the shape of the body must be geometrically unchanged and back-scattered field is then zero. This means that if EM wave is incident along the axis of symmetry of a body, then geometric requirements of the theorem are satisfied, and the body has the relative permeability and permittivity which must be equal ($\mu_r = \varepsilon_r$). [16,23]

The second Weston`s theorem is about surface impedance. When incoming EM wave is an incident upon medium, a total tangential electromagnetic field components can satisfy the impedance boundary condition (as stated on the equation (12)) [16], and the surface of the body is invariant by the 90-degree rotation. The far-zone of backscattering field will be zero if the direction of incidence is along the axis of body. It complies with the equation (18) because

surface impedance η_s and characteristic impedance of free space η_0 are equal. This leads to normalized surface impedance (Z_S) being equal to one. [16,23]

To solve the surface impedance in ohms, it can be expressed as in equation (12) [16,23]:

$$\eta_s = \frac{E_{tan}}{H_{tan}}, \tag{12}$$

where E_{tan} is a tangential component of electric field and H_{tan} is a tangential component of magnetic field. Both these components can be written as in equations (13-14):

$$|E_{tan}| = \vec{E}_i + \vec{E}_s, \tag{13}$$

$$|H_{tan}| = \vec{H}_i + \vec{H}_s, \tag{14}$$

where *i* and *s* are incident and scattering terms of the tangential component of the electric and magnetic fields vectors.

By using the equation (15) for the electric field current, and the equation (16) for magnetic field currents, following expression can be derived (equation (17))[16]:

$$\vec{E} - n_{unit}\left(n\vec{E}\right) = \eta_s n_{unit} \times \vec{H} = \eta_s \vec{J_s}, \tag{15}$$

$$\vec{H} - n_{unit}\left(n\vec{H}\right) = -\frac{1}{\eta_s} n_{unit} \times \vec{E} = \frac{1}{\eta_s}\overrightarrow{J_{ms}}, \tag{16}$$

$$\overrightarrow{-J_{ms}} = \eta_s n_{unit} \times \vec{J_s} \tag{17}$$

where n_{unit} is a unit outward normal to the surface, $\vec{J_s}$ is surface current source and $\overrightarrow{J_{ms}}$ is magnetic surface current source.

Frequently, the normalized surface impedance is used, which is defined as in equation (18) [16]:

$$Z_s = \frac{\eta_s}{\eta_0}, \tag{18}$$

To calculate characteristic impedance of free space, first equation (19) should be considered [16]:

$$\eta_s = \frac{E_{tan}}{H_{tan}} = \eta \tag{19}$$

where are used tangential electric field is in (expressed in Volts per meter (V m^{-1})) and tangential magnetic field in (expressed in Amperes per meter (A m^{-1})).

If both tangential fields are satisfied (as described in Weston´s theorem 2), then the Equation 20 [16] is valid:

$$\eta_0 = \sqrt{\frac{\mu_0}{\varepsilon_0}}, \tag{20}$$

where characteristic impedance of free space is equal to $120\pi \approx 377\ \Omega$.

3 ABSORBER MATERIALS MEASUREMENT METHODS THEORY

The Vector Network Analyzer (VNA) is a measurement device that measures network parameters of materials, components, or devices. VNA is one of the most important tools for the telecommunications engineering and in microelectronics industries. VNA has become a popular tool because it can be used to measure reflection and transmission, at high frequencies, [24] or even amplitudes and phases of the waves.

3.1 Matrixes and Scattering parameters

VNA expresses results in scattering matrixes (S-matrix) which are a mathematical description of a material or a device [24]. By using S-matrix parameters, for example, relative complex permeability and permittivity of materials can be solved. The measured S-matrices contain information about attenuation characteristics material on how well electronic waves are reflected and how much propagates through the samples, and what is transmitted back to the device [24].

From equation (21) [19,24] it can be observed, for example, how many ports the network has.

$$[S] = \begin{pmatrix} S_{11} & S_{12} & \dots & S_{1N} \\ S_{21} & \ddots & & \vdots \\ \vdots & & \ddots & \vdots \\ S_{N1} & \dots & \dots & S_{NN} \end{pmatrix}, \tag{21}$$

S-matrix for a VNA with 2-ports would look like in the equation (22) [19,24]:

$$[S] = \begin{pmatrix} S_{11} & S_{12} \\ S_{21} & S_{22} \end{pmatrix}, \tag{22}$$

where S_{11} and S_{22} scattering parameters represent the reflection coefficients, S_{12} and S_{21} are scattering parameters for the transmission coefficients, respectively.

The transmission and reflection coefficients are backed up with the wave incidents at the ports 1 and 2. This can be seen from the equation (23) [24]:

$$\begin{pmatrix} V_1^- \\ V_2^- \\ \vdots \\ V_N^- \end{pmatrix} = \begin{pmatrix} S_{11} & S_{12} & \dots & S_{1N} \\ S_{21} & \ddots & & \vdots \\ \vdots & & \ddots & \vdots \\ S_{N1} & \dots & \dots & S_{NN} \end{pmatrix} \begin{pmatrix} V_1^+ \\ V_2^+ \\ \vdots \\ V_N^+ \end{pmatrix}, \tag{23}$$

where V_N^+ is an amplitude of the voltage transmitted and V_N^- is an amplitude of the voltage reflected.

But because the above-mentioned is for 2-port, it can be rewritten into the equation (24) [19,24] format:

$$\begin{pmatrix} V_1^- \\ V_2^- \end{pmatrix} = \begin{pmatrix} S_{11} & S_{12} \\ S_{21} & S_{22} \end{pmatrix} \begin{pmatrix} V_1^+ \\ V_2^+ \end{pmatrix}, \tag{24}$$

From the equation (24), scattering parameters for reflection and transmission coefficients can be expressed by using the equations (25-28) [19].

$$S_{11} = \frac{V_1^-}{V_1^+}, \quad (25)$$

$$S_{12} = \frac{V_1^-}{V_2^+}, \quad (26)$$

$$S_{21} = \frac{V_2^-}{V_1^+}, \quad (27)$$

$$S_{22} = \frac{V_2^-}{V_2^+}, \quad (28)$$

Furthermore, it can be seen that waves are transmitted and reflected at each port (Figure 4). The S_{11} is a reflection that is seen from the port 1 to 2, while S_{22} is a reflection seen from the port 2 to 1. Correspondingly, S_{12} and S_{21} are the transmissions seen from the ports 2 to 1 and from 1 to 2, respectively.

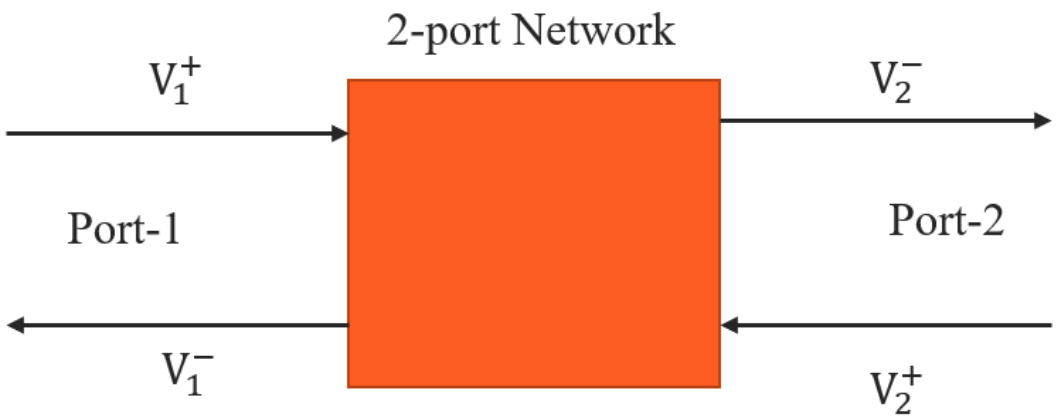

Figure 4. Two-port network which is assumed to be passive and linear.

3.2 Waveguide

In a waveguide, the electromagnetic radiation is guided through the transmission line. The waveguide can be, for example, a hollow waveguide, a coaxial-cable, or a micro-strip, while dielectric waveguides are referred as optical fibres or integrated waveguides [25]. A waveguide consists of a hollow metallic tube with a uniform cross section that transmits the electromagnetic waves by reflections from the inner walls of the tube [26]. The waveguide measurements are usually done in microwave frequencies ranging from 300 MHz to 300 GHz.

3.2.1 Rectangular waveguide

Although, there are multiple different type of waveguides with distinct shape (e.g., circular, elliptical, single, or double ridged, and rectangular) [25,26], the interest in most cases is the rectangular waveguide. The rectangular waveguide has multiple different types of waveguides such as ridge, bulge, or immersed guide, etc [25]. For example, the immersed waveguide is a hollow while the outer shell is made of metallic materials (e.g., copper, silver, or gold) [26]. The rectangular waveguides support transverse magnetic (TM) and transverse electric (TE) modes but does not support transverse electromagnetic (TEM) mode [25,27]. Because the hollow guide does not have an inner conductor, it is impossible to define a voltage by only having one conductor due the Maxwells equations [28].

If the frequency is not correct for the waveguide, then EM waves will not propagate inside the hollow shell of the waveguide. Thus, the waveguide acts as a high pass filter which means that the transmitted EM radiation is too low as it decays very rapidly in a direction of the waveguide axes [29]. If the frequency is chosen correctly, the EM radiation will pass through the waveguide [29]. The lowest frequency at which the propagation is possible is called a cut-off frequency. When the frequency is higher than the cut-off frequency, the rectangular waveguide can have both TE and TM modes [25]. Figure 5 shows how waves propagate when the frequency is barely, or far above, the cut-off frequency (which is determined geometrically) [27,30]. It is clearly seen that when the frequency is increased, the wavelength increases [27,29].

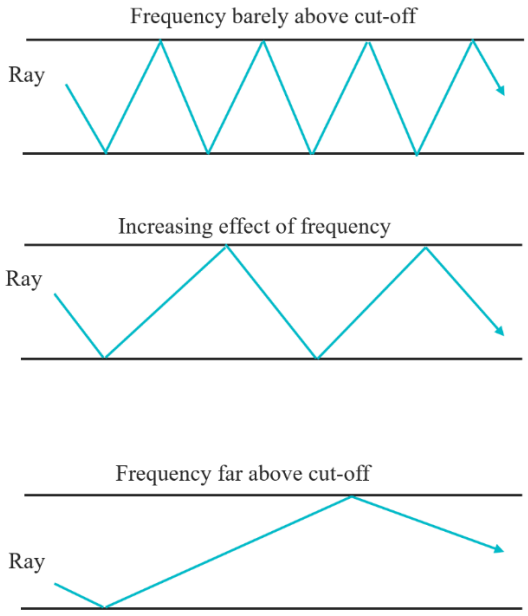

Figure 5. Wavelength increases with the frequency.

3.2.2 Cut-off frequency

The cut-off frequency (f_c) can be calculated from the equation (29) [27–30]:

$$f_c = \frac{1}{2\pi\sqrt{\mu\varepsilon}}\sqrt{\left(\frac{m\pi}{a}\right)^2 + \left(\frac{n\pi}{b}\right)^2}, \quad (8)$$

where ε is a permittivity, μ is a permeability, n is a number of half-cycle variations of the fields in the y-direction, m is a number of half-cycle variations of the fields in the x-direction, a corresponds to an x-axis length of the waveguide, and b for a y-axis length of waveguide [28]. The cross-sectional dimensions of the waveguide play a huge role in the cut-off frequency, because the larger dimensions lead to lower the cut-off frequency [29]. This explains why the cross-sectional dimensional of the waveguide are related to the measurement frequency range.

From the equation (29) it can be seen that there are issues related the permittivity and permeability, but these are usually ε_0 and μ_0.Thus this equation can be rewritten to equation (30) [27,29,30]:

$$c = \frac{1}{\sqrt{\varepsilon_0\mu_0}} \rightarrow f_c = \frac{c}{2}\sqrt{\left(\frac{m}{a}\right)^2 + \left(\frac{n}{b}\right)^2}, \quad (30)$$

where c is a speed of light (299 792 458 m s^{-1})

By knowing a, b, n and m can the cut-off wavelength λ_c be solved as shown in equation (31) [27,29].

$$\lambda_c = \frac{c}{f_c} \rightarrow \lambda_c = \frac{2}{\sqrt{\left(\frac{m}{a}\right)^2 + \left(\frac{n}{b}\right)^2}} = \frac{2ab}{\sqrt{m^2b^2 + n^2a^2}}, \quad (31)$$

3.2.3 TM mode

Waveguide uses EM waves [26,27], that compose of electric and magnetic fields that propagate perpendicularly to each other in the same direction [27]. If both fields are in that way, then it would be TEM mode, but because in this case it cannot happen as mentioned before [27]. Figure 6 shows how a TM mode works and it can be seen that electric fields of the waves have beginning and end points into direction of usual wave propagation, while magnetic fields waves are shown as continuous loops that are traverse to the direction of the propagation wave [25,27].

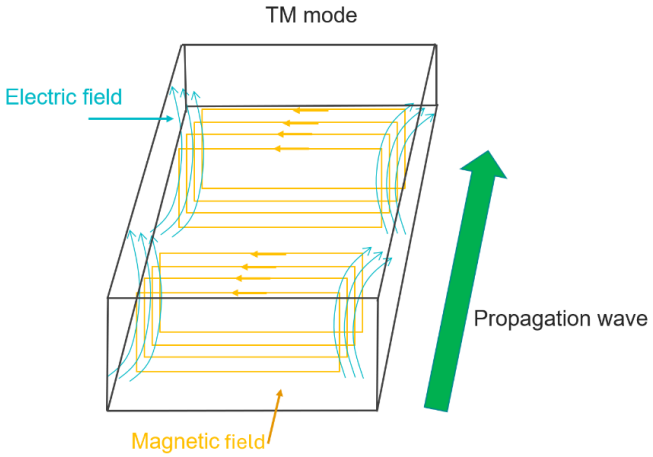

Figure 6. Transverse magnetic (TM) mode which shows the magnetic and electric fields in relation to the propagation of EM waves.

3.3 Conversion methods

There are four common conversion methods for S-parameters to calculate the dielectric and/or magnetic properties of materials. These are known as Nicolson-Ross-Weir (NWR), Short-Circuit Line (SCL), a new non-iterative, and NIST iterative methods [31]. The NRW method is the most widely used [32]. In these four conversion methods are simultaneously measured complex transmission and reflection coefficients, for the material in the transmission line [32], as can be seen from Table 1.

Table 1. The common conversion methods, and the properties that can be calculated from the S-parameters.

Conversion method	S-parameters	Dielectric properties
NRW	$S_{11}, S_{21}, S_{12}, S_{22}$ or S_{11}, S_{21}	ε_r, μ_r
SCL	S_{11}	ε_r, μ_r
New non-iterative	$S_{11}, S_{21}, S_{12}, S_{22}$ or S_{11}, S_{21}	ε_r $(\mu_r = 1)$
NIST iterative	$S_{11}, S_{21}, S_{12}, S_{22}$ or S_{11}, S_{21}	ε_r $(\mu_r = 1)$

3.3.1 Nicolson-Ross-Weir method

The Nicolson-Ross-Weir method can provide direct calculations from waveguide results by using the scattering parameters S_{11}, S_{12}, S_{21} and S_{22} obtained from the 2-port measurements. [32]

To calculate needed relative permittivity and relative permeability the S-parameters must be solved first. The functions for S-parameters are shown in equations (32-33) [31–34]:

$$S_{11} = \frac{(1-T^2)\Gamma}{1-T^2\Gamma}, \tag{32}$$

$$S_{21} = \frac{(1-\Gamma^2)T}{1-T^2\Gamma^2}, \tag{33}$$

where Γ is reflection coefficient and T is transmission coefficient. The equation (32) is for reflected signal while (33) is for transmitted signal.

First needs to be solved X product, which is done with equation (34):

$$X = \frac{{S_{11}}^2 - {S_{21}}^2 + 1}{2S_{11}}, \tag{34}$$

where are used scattering parameters S_{11} and S_{21}. The X is an intermediate product. In the reflection coefficient must be remembered that sign is chosen by condition $|\Gamma| < 1$ [31], because the reflection coefficient cannot be greater than 1 due Smith chart conditions.

To solve needed reflection and transmission coefficients it can be done by using equations (35-36) [31–34]:

$$\Gamma = X \pm \sqrt{X^2 - 1}, \tag{35}$$

$$T = \frac{S_{11}+S_{21}-\Gamma}{1-(S_{11}+S_{21})\Gamma}, \quad (36)$$

The transmission coefficient in equation (36) can be solved by equation (37) [33,34]:

$$T = e^{-\gamma * l}, \quad (37)$$

where γ is propagation constant, e is a Euler's number and l is length in meters.

To solve in equations (37) propagation constant can be used equations (38) [34]:

$$\gamma = j\frac{2\pi}{\lambda_0}\sqrt{\varepsilon_r\mu_r - \left(\frac{\lambda_0}{\lambda_c}\right)^2}, \quad (38)$$

where λ_0 is free space wavelength, λ_c is cut-off wavelength ε_r relative permittivity and μ_r is relative permeability.

In case of empty waveguide, then the equation (38) can be written into equation (39) [34]:

$$\gamma_0 = j\frac{2\pi}{\lambda_0}\sqrt{1 - \left(\frac{\lambda_0}{\lambda_c}\right)^2}, \quad (39)$$

where γ_0 is propagation constant of free space.

Then next parameter to solve would be loaded guided wavelength (denoted as *Λ)* in equation (40) [34]:

$$\Lambda = \frac{\lambda_0}{\sqrt{\varepsilon_r\mu_r - \left(\frac{\lambda_0}{\lambda_c}\right)^2}}, \quad (40)$$

The issue with the equation (40) is that to solve the relative permittivity and permeability, the equation for loaded guided wavelength needs a bit different approach. For this reason, the equation (37) for transmission coefficient is combined with the new equation (41) [31,33] (for propagation constant) to form the equation (42) [31,33,34]:

$$\gamma = j\frac{2\pi}{\Lambda}, \quad (41)$$

$$T = e^{-j\frac{2*\pi}{\Lambda}l}, \quad (42)$$

By using rules related to natural logarithm, the equation (42) be transformed into the equations (43-44) [31,33,34]:

$$-j\frac{2\pi}{\Lambda}l = ln(T) \rightarrow -j2\pi l = ln(T)\Lambda \quad (43)$$

$$-j\frac{2\pi l}{ln(T)} = \Lambda \rightarrow \frac{1}{\Lambda} = \frac{j}{2\pi l}ln(T) \quad (43)$$

The last variable before the relative permittivity and permeability can be solved, is the guided wavelength related to the empty waveguide, which is shown in the equation (45) [34]:

$$\lambda_{0g} = \frac{\lambda_0}{\sqrt{1-\left(\frac{\lambda_0}{\lambda_c}\right)^2}} \; or \; \lambda_{0g} = \frac{1}{\sqrt{\frac{1}{\lambda_0{}^2}-\frac{1}{\lambda_c{}^2}}}, \tag{45}$$

where λ_{0g} is an empty guided wavelength.

Now, the relative permeability can be solved from the equation (46) [31,33,34]:

$$\mu_r = \frac{\lambda_{0g}}{\Lambda}\frac{(1+\Gamma)}{(1-\Gamma)}, \tag{46}$$

The relative permittivity can be solved from the equation (47) [31,33,34]:

$$\varepsilon_r = \frac{\lambda_0{}^2}{\mu_r}\left(\frac{1}{\Lambda^2}+\frac{1}{\lambda_c{}^2}\right) \tag{47}$$

3.3.2 Short circuit line method

Another way to calculate a relative permittivity and a permeability of a material is to use a short circuit line (SCL) method. The SCL is an iterative method that uses only one of the scattering parameter S_{11}. So, the SCL calculations are possible with one-port measurement [31] in consideration of the matching boundary conditions in the field equations [7].

Solving the permittivity and the permeability value of a material starts by obtaining a phase (*Q*) from the equation (48) [7,31]:

$$Q = e^{-2*\gamma_0*L}, \tag{48}$$

where *L* is a distance from a short circuit to a sample and γ_0 is a propagation constant in a free space solved by the Equation (49):

$$\gamma_0 = j\sqrt{\frac{\omega^2\mu_r\varepsilon_r}{c^2}-\left(\frac{2\pi}{\lambda_c}\right)^2} = j\sqrt{\left(\frac{\omega}{c}\right)^2-\left(\frac{2\pi}{\lambda_c}\right)^2}, \tag{49}$$

where λ_c is a cut-off wavelength, c is a speed of light, μ_r is a relative permeability and ε_r is a relative permittivity. Because this equation is for free space (μ_r =1, ε_r =1), the equation can be reduced as shown.

By knowing the propagation constant in the material and the propagation constant in the free space, the Equation (50) be formed [7,31]:

$$B = \frac{\gamma \mu_0}{\gamma_0 \mu_r}, \tag{50}$$

where B is an effective impedance.

To calculate the relative permittivity and the permeability from the short circuit, positions at the same frequency (p) are needed as shown in the Equations (51-52) [7,31]:

$$p_1 = \frac{2B\,Q_1 - [(Q_1+1)+(Q_1-1)B^2]\tanh(\gamma L)}{-2B+[(Q_1-1)B^2+(Q_1+1)]\tanh(\gamma L)}, \tag{51}$$

$$p_2 = \frac{2B\,Q_2 - [(Q_2+1)+(Q_2-1)B^2]\tanh(\gamma L)}{-2B+[(Q_2-1)B^2+(Q_2+1)]\tanh(\gamma L)}, \tag{52}$$

where p_1 is the first position and p_2 is the second position in the short circuit.

By noting the unity between the scattering parameter S_{11} and the position, the result will be Equation (53) [7]:

$$S_{11} = p = \frac{-2BQ + [(Q+1)+(Q-1)B^2]\tanh(\gamma L)}{-B+[(Q+1)-(Q-1)B^2]\tanh(\gamma L)}, \tag{53}$$

Now after knowing the positions (p_1, p_2), and phases from the previous equations, the propagation constant of the material (γ) can be solved from the equations (54-55) [7]:

$$\tanh(\gamma L) = \frac{2B(Q_1+p_1)}{B^2(p_1+1)(Q_1-1)+(1-p_1)(1+Q_1)}, \tag{54}$$

$$\gamma = \frac{1}{L}\left(\tanh^{-1}\left(\left[\frac{2B(Q_1+p_1)}{B^2(p_1+1)(Q_1-1)+(1-p_1)(1+Q_1)}\right] + 2\pi n_{int} j\right)\right), \tag{55}$$

where n_{int} is an integer determined from a group delay, and phases Q_1 and Q_2 from the positions p_1 and p_2 (both have the same distance from the short circuit to the sample).

The constant B can be solved from the equation (56), and later used in the equation (54) to find the relative permittivity and the permeability of the material [7]:

$$B^2 = \frac{Q_1(Q_2(p_1-p_2)+p_1p_2+1-2p_2)-(Q_2(p_1(p_2-2)+1)+p_2-p_1)}{Q_1(Q_2(p_1-p_2)+p_1p_2+1-2p_2)-(Q_2(p_1(p_2+2)+1)+p_2-p_1)}, \tag{56}$$

4 CACLULATION THEORY

In this section, an attenuation constant, characteristic input impedance, a reflection loss and electromagnetic shielding effectiveness values will be explained. The focus of this part is to provide a further discussion of the meaning of these parameters and properties, and how they can be solved for a characterized material.

4.1 Attenuation constant

Transmissions lines are designed to guide electromagnetic waves, but losses always exist [16]**[1]**. With the geometry, dimensions, and materials at the transmission line it is possible to determinate an attenuation constant (α) [16], which also referred as an attenuation factor. The α is expressed as neper per meter (Np m^{-1}). The α is the real part of propagation constant (γ) , while the imaginary part of propagation constant is known as the phase constant (β) (expressed as $\gamma = \alpha + \beta j = j\omega\sqrt{\mu_r \varepsilon_r}$) [16]. The α determinates the attenuation properties of the material **[12]**, and the value can be solved with transmission line theory.

4.1.1 Calculating the attenuation constant

The α can be solved after obtaining ε_r and μ_r values from the S-parameters. With the knowledge that both consist of real and imaginary parts, the equations (57-58) can be formed [35]:

$$\delta' = \mu'\varepsilon' - \mu''\varepsilon'', \tag{57}$$

$$\delta'' = \mu'\varepsilon'' + \mu''\varepsilon', \tag{58}$$

where δ'' acts as divided part and δ' as divider part in loss tangent $tan(\delta)$ for an electric and magnetically lossy material as shown in the equations (59-60) [35]:

$$tan(\delta) = \frac{\delta''}{\delta'}, \tag{59}$$

$$tan(\delta) = \frac{\mu'\varepsilon'' + \mu''\varepsilon'}{\mu'\varepsilon' - \mu''\varepsilon''}, \tag{60}$$

where μ' and ε' are the real parts of the relative permeability and permittivity, respectively, while $\mu''$and ε'' are the imaginary parts of relative permeability and permittivity, respectively.

At the beginning, α can be represented as in the equation (61) [35]:

$$\alpha = \frac{\pi\sqrt{2\delta'}}{\lambda_0}\sqrt{\sqrt{1 + tan(\delta)^2} - 1}, \tag{61}$$

where λ_0 is a free space wavelength. The λ_0 can be written as $\lambda_0 = c/f$. Thus, the above-mentioned equation can be rewritten by using the equations (57) and (60) (as shown in the equations (62-64)) [35]:

$$\alpha = \frac{\sqrt{2}\pi}{\frac{c}{f}}\sqrt{\delta'}\sqrt{\sqrt{1+tan(\delta)^2}-1}, \tag{62}$$

$$\alpha = \frac{\sqrt{2}\pi f}{c}\sqrt{\delta'}\sqrt{\sqrt{1+\left(\frac{\delta''}{\delta'}\right)^2}-1}, \tag{63}$$

$$\alpha = \frac{\sqrt{2}*\pi*f}{c}(\mu'\varepsilon' - \mu''\varepsilon'')\sqrt{\sqrt{1+\left(\frac{\mu'\varepsilon''+\mu''\varepsilon'}{\mu'\varepsilon'-\mu''\varepsilon''}\right)^2}-1}, \tag{64}$$

The equation (64) can be now rewritten into a more appropriate format as shown in the equations (65-69) [12,35–39]:

$$\alpha = \frac{\sqrt{2}\pi f}{c}\sqrt{\delta'\sqrt{\frac{\delta'^2+\delta''^2}{\delta'^2}}-1}\alpha = \frac{\sqrt{2}\pi f}{c}\sqrt{\delta'\frac{\left(\sqrt{\delta'^2+\delta''^2}-\delta'\right)}{\delta'}}, \tag{65}$$

$$\alpha = \frac{\sqrt{2}\pi f}{c}\sqrt{\sqrt{\delta'^2+\delta''^2}-\delta'}, \tag{66}$$

$$\alpha = \frac{\sqrt{2}\pi f}{c}\sqrt{\sqrt{(\mu'\varepsilon' - \mu''\varepsilon'')^2+(\mu'\varepsilon''+\mu''\varepsilon')^2}-(\mu'\varepsilon' - \mu''\varepsilon'')}, \tag{67}$$

$$\alpha = \frac{\sqrt{2}\pi f}{c}\sqrt{(\mu''\varepsilon'' - \mu'\varepsilon') + \sqrt{(\mu'\varepsilon' - \mu''\varepsilon'')^2+(\mu'\varepsilon''+\mu''\varepsilon')^2}}, \tag{68}$$

$$\alpha = \frac{\sqrt{2}\pi f}{c}\sqrt{(\mu''\varepsilon'' - \mu'\varepsilon') + \sqrt{(\mu''\varepsilon'' - \mu'\varepsilon')^2+(\mu'\varepsilon''+\mu''\varepsilon')^2}}, \tag{69}$$

As shown in the equation (68), it can be seen that there is exist a term $(\mu'\varepsilon' - \mu''\varepsilon'')^2$. For the equation (69), the same part is expressed in a form $(\mu''\varepsilon'' - \mu'\varepsilon')^2$. This does not pose any problems because the end result will be the same due the exponent calculations.

4.2 Reflection loss

The main idea of TL theory is that the plane EM wave problem can be replaced by an equivalent TL problem that simplifies the solution to calculate the reflection loss (RL) [1]. Usually, a transmissions line consists of two conductors, and these transmission lines can be, for example, coaxial lines or strip-lines. The Maxwell's equations for EM wave propagation use the EM fields that can be derived from the Ampere's law of circle integral and Faraday's law of induction [1].

4.2.1 Characteristic input impedance

To determine RL, both the characteristic input impedance of a medium (η_{in}) and the characteristic impedance of free space (η_0) must be known. The η_0 was already explained earlier by using the Weston´s theorem (in the section 2.3.4).

Solving η_{in} can be done with the equation (70) [40]:

$$\eta_{in} = \eta_0 \eta tanh(\gamma t), \tag{70}$$

where η is an electromagnetic wave characteristic impedance, and t is a thickness of the material.

The η can be written as in the equation (71) [40]:

$$\eta = \sqrt{\frac{\mu_r}{\varepsilon_r}} = \sqrt{\frac{\mu' - \mu'' j}{\varepsilon' - \varepsilon'' j}}, \tag{71}$$

While the γ can be expressed as in the equation (72) [40]:

$$\gamma = j\frac{2\pi}{\lambda_0}\sqrt{\mu_r \varepsilon_r} = \frac{2\pi f}{c}\sqrt{\mu_r \varepsilon_r}, \tag{72}$$

When combining the equations (71-72) with the equation (70), it will result into the equation (73) [12,35,37,39,40]:

$$\eta_{in} = \eta_0 \sqrt{\frac{\mu_r}{\varepsilon_r}} tanh\left(j\frac{2\pi f}{c} t\sqrt{\mu_r \varepsilon_r}\right), \tag{73}$$

This gives the η_{in} as a final product in a complex format. The impedance ratio can be expressed as η_{in}/η_0 which indicates the matching condition of an electromagnetic absorber.

4.2.2 Reflection coefficient and reflection loss

The reflection coefficient (often written as Γ) is a ratio of the amplitude of a reflected field and an amplitude of an incident field (in which both the magnitude and the phase are included). The Γ may also indicate a ratio of a reflected signal voltage to that of an incident signal voltage.

The Γ can be calculated by using the impedances (η_{in} and η_0) as seen in the equation (74).

$$\Gamma = \frac{\eta_{in} - \eta_0}{\eta_{in} + \eta_0} \tag{74}$$

By integrating Γ with the logarithm, RL can be calculated from the equation (75) [12,35–37,39,40]:

$$RL = 20log_{10}|\Gamma| = 20log_{10}\left|\frac{\eta_{in} - \eta_0}{\eta_{in} + \eta_0}\right|, \tag{75}$$

where RL as a final product expressed as decibels (dB).

4.3 Shielding effectiveness

4.3.1 Total shielding effectiveness

The shielding effectiveness (referred as SE) is often related to far-fields in which the attenuation is dependent on the properties of a medium through which the electromagnetic wave is propagating. The total SE (SE_T; expressed in dB) can be written using the magnetic and electric fields [4] as shown in the Equations (76-77) [3,4]:

$$SE_T = 20log_{10}\left(\frac{E_i}{E_t}\right), \tag{76}$$

$$SE_T = 20log_{10}\left(\frac{H_i}{H_t}\right), \tag{77}$$

where E_i and H_i are incident electric and magnetic fields, while respectively E_t and H_t are transmitted electric and magnetic fields.

By using the equation (76), the total shielding effectiveness can be rewritten into the equation (78) that consist of three components [3,4]:

$$SE_T = SE_M + SE_R + SE_A, \tag{78}$$

where SE_M is shielding through multiple internal reflections, SE_R is shielding through reflection and SE_A is shielding through absorption. The reflection is caused by the reflection at the material interfaces, while absorption represents the attenuation that the incident wave experiences as it propagates through the shield [3].

4.3.2 Shielding by multiple reflections

In thin shielding structures, when a reflected wave from the second boundary gets reflected in the first boundary, it goes back to the second boundary where it again gets reflected. If the shield is thick or quantity of the boundaries is small, this can be neglected. [4] (As observed in Figure 7.) From an electric field perspective, the incident wave gets mostly reflected at the first boundary and only a small fraction enters inside the shield. Meanwhile, from a magnetic field perspective, most of the incident wave passes into the shield at the first boundary. [4]

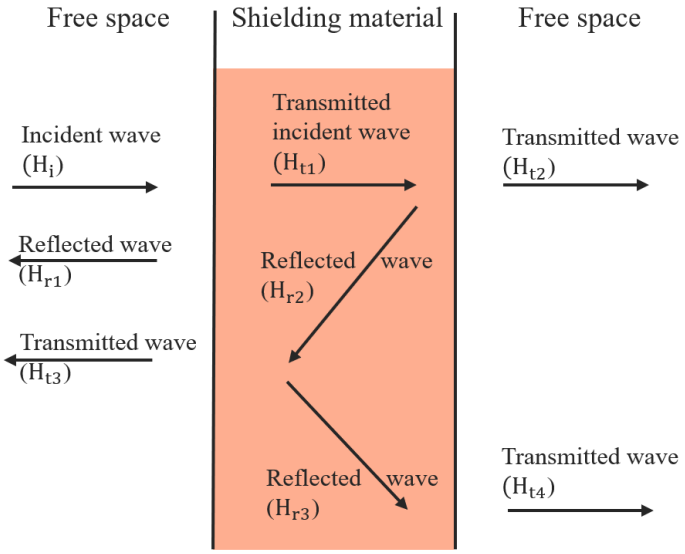

Figure 7. Schematic illustration of the mechanisms of multiple reflections.

The attenuation that propagating EM waves experiences in a medium can be written as in the equation (79). In the case of a good conductor, the attenuation is highly dependent on the skin depth of the shield. Now if the thickness of the shield is assumed to be much smaller than the skin depth and the η_0 must be significantly greater than the η [3], an approximation for the multiple reflections can be made (shown in the equation 84) by using the equations (79-83) [3].

$$e^{-\gamma t} = e^{-\alpha t} e^{-j\beta t}, \tag{79}$$

where γ is a propagation constant (expressed as $\alpha + i\beta$), t is a thickness of a shield (in metres), α is an attenuation constant (in nepers per meter), and β is a phase constant (in radians per meter).

$$\beta = \alpha = \frac{1}{\delta}, \tag{80}$$

$$e^{-\gamma t} = e^{-\frac{t}{\delta}} e^{-j\frac{t}{\delta}} \ll 1 \text{ for } t \gg \delta, \tag{81}$$

$$\frac{\eta_0 - \eta}{\eta_0 + \eta} = 1, \tag{82}$$

$$SE_M = 20\log_{10}\left(\left|1 - \left(\frac{\eta_0 - \eta}{\eta_0 + \eta}\right)^2 e^{\frac{-2t}{\delta}} e^{j\frac{-2t}{\delta}}\right|\right), \tag{83}$$

$$SE_M = 20\log_{10}\left(\left|1 - e^{\frac{-2t}{\delta}} e^{j\frac{-2t}{\delta}}\right|\right), \tag{84}$$

SE_M value can be usually neglected as the thickness is close to or greater than the skin depth of the shield [3,4,41]. A good rule of thumb is that when SE_A is greater than ≈ 9 dB, the value of SE_M has negligible contribution to the SE_T value [4,42].

4.3.3 Shielding by reflection

The reflection is due impedance mismatch at the air-material interface [4]. By using the magnetic and electric fields for incident waves (H_i and E_i) and intensities of the transmitted waves (H_t and E_t) [3,4], the reflection can be solved. By looking at the Figure 8, two different boundaries can be seen. The first boundary is when the incident wave penetrates to the shield from the left side, and the second boundary is when the wave leaves the shield from the right side [3]. As a result, the first boundary can be written as in the equation (85) and for the second boundary as in the equation (86) [3,4]:

$$\frac{E_1}{E_i} = \frac{2\eta}{\eta_0+\eta}, \tag{85}$$

$$\frac{E_t}{E_1} = \frac{2\eta_0}{\eta_0+\eta}, \tag{86}$$

where in the first boundary the incident wave at the start is E_i and inside the shield is the transmitted wave E_1, while for the second boundary now the incoming wave is the E_1 wave, that then goes through the shield's right side, and as the result, the new final transmitted wave becomes known as E_t [3,4].

It is important to note that for the first boundary the incident wave impedance is η_0, while for the transmitted wave it is now η [3]. While at the second boundary, the incident wave impedance is now η, and for the transmitted wave impedance is now η_0 (Figure 8). As a result, the transmission coefficient can be expressed as in the equation (87): [3]

$$\frac{E_t}{E_i} = \frac{E_1}{E_i}\frac{E_t}{E_1} = \frac{2\eta_0}{\eta_0+\eta}\frac{2\eta}{\eta_0+\eta} = \frac{4\eta_0\eta}{(\eta_0+\eta)^2}, \tag{87}$$

Because in the equation (85) $\eta_0 \gg \eta$ is smaller compared to equation (86). It results that at the first boundary the transmission coefficient is very small, while at second boundary it is around 2. This is why most of electric field is transmitted through the first boundary. In the first boundary the reflection coefficient is -1, while at the second boundary it is +1. This is analogous to the reflections at the end of left boundary or at the right boundary at transition line. Thus, only small portion of electric field manages to pass through the first boundary. This small amount of electric field passing through the first boundary results in reflection at the second boundary. As a result, the reflection can be calculated as shown in the equation (88): [3,4]

$$SE_R = 20log_{10}\left|\left(\frac{E_i}{E_t}\right)\right|, \tag{88}$$

The SE_R can be written as in the equation (91) by considering the equations (89-90) [3]:

$$SE_R = 20\,log_{10}\left|\frac{(\eta_0+\eta)^2}{4\eta_0\eta}\right| = 20\,log_{10}\left|\frac{\eta_0}{4\eta}\right|, \tag{89}$$

The SE_R can be written as in the equation (91) by considering the equation (90) information in equation (89) [3]:

$$\eta = \sqrt{\frac{\omega\mu}{\sigma}} \; and \; \eta_0 = \sqrt{\frac{\mu_0}{\varepsilon_0}}, \tag{90}$$

$$SE_R = 20\, log_{10}\left(\frac{1}{4}\sqrt{\frac{\sigma}{\omega\mu_r\varepsilon_0}}\right), \tag{91}$$

From the above-mentioned equations, it can be seen that the SE_R can be calculated by using an electric field without magnetic field. The equations are similar. However, there is a one important difference which is that transmission of magnetic field occurs on the first boundary, while for the electric field it occurs at the second boundary [3]. This can be observed from the equations (85-86) and (92-96) [3]. Therefore, the attenuation of the magnetic field at the boundary is more important than attenuation of electric field [3]. The thicker the medium is, the more effect the boundary will have against magnetic fields than on electric fields [3].

$$\frac{H_1}{H_i} = \frac{\frac{E_1}{\eta}}{\frac{E_i}{\eta_0}} \rightarrow \frac{H_1}{H_i} = \frac{E_1}{E_i}\frac{\eta_0}{\eta}, \tag{92}$$

$$\frac{H_1}{H_i} = \frac{2\eta_0}{\eta_0+\eta}, \tag{93}$$

$$\frac{H_t}{H_1} = \frac{\frac{E_t}{\eta_0}}{\frac{E_1}{\eta}} \rightarrow \frac{H_1}{H_i} = \frac{E_t}{E_1}\frac{\eta}{\eta_0}, \tag{94}$$

$$\frac{H_1}{H_i} = \frac{2\eta}{\eta_0+\eta}, \tag{95}$$

$$\frac{H_t}{H_i} = \frac{H_1}{H_i}\frac{H_t}{H_1} = \frac{2\eta_0}{\eta_0+\eta}\frac{2\eta}{\eta_0+\eta} = \frac{4\eta_0\eta}{(\eta_0+\eta)^2}, \tag{96}$$

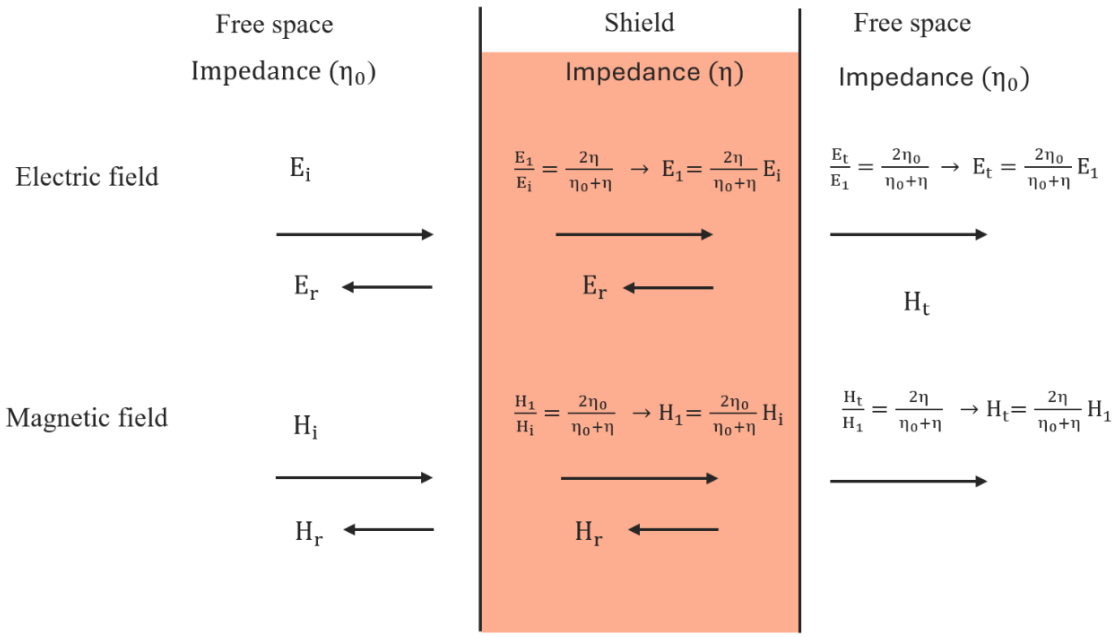

Figure 8. Schematic illustration of the boundary conditions.

4.3.4 Shielding effectiveness by absorption

The shielding effectiveness by absorption (SE_A) can be solved by using electric and magnetic fields. The currents induced in the shield produce ohmic losses and heating of the material [3]. As EM wave goes through a medium, the amplitude decreases exponentially dependent on the intrinsic properties of the shield [3]. Thus, SE_A value can be determined by using the equations (98-99) [4] and (100-101) [3,4,43]:

$$E_t = E_i e^{-\frac{t}{\delta}}, \tag{98}$$

$$H_t = H_i e^{-\frac{t}{\delta}}, \tag{99}$$

$$SE_A = 20log_{10}\left(e^{\frac{t}{\delta}}\right) = 20\frac{t}{\delta}log_{10}(e), \tag{100}$$

$$SE_A = 8.686\frac{t}{\delta}, \tag{101}$$

where t is a thickness of a shield, δ is a skin depth, E_i and E_t are incident and transmitted electric fields, respectively, H_i and H_t are incident and transmitted magnetic fields, respectively.

4.3.5 Shielding effectiveness from waveguide measurements

Components to calculate the total shielding effectiveness can be obtained from the S-parameters (S_{11}, S_{11}, S_{21} and S_{22}). By using knowledge of the electric fields, the transmission (T) and reflection coefficients (R) can be written as in the equations (102-103) [42]:

$$T = \left|\frac{E_t}{E_i}\right|^2 = |S_{21}|^2 = |S_{12}|^2, \quad (102)$$

$$R = \left|\frac{E_r}{E_i}\right|^2 = |S_{11}|^2 = |S_{22}|^2, \quad (103)$$

where E_t and E_i refers to transmitted and incident wave in electric field, respectively, S_{21} and S_{12} are the scattering parameters for the transmitted signal, E_r is a reflected wave in electric field, and S_{11} and S_{22} are the scattering parameters for reflected signal.

By using the knowledge of *T* and *R,* it is then possible to determine the absorption coefficient (A) with the equation (104) [42,44,45]:

$$\mathrm{R} + \mathrm{A} + \mathrm{T} = 1 \rightarrow A = 1 - T - R, \quad (104)$$

Now the shielding effectiveness for the absorption (the equation (105)) and the reflection (the equation (106)) can be solved in decibels [42,44,45]:

$$SE_A = 10\log_{10}\left|\frac{1-R}{T}\right| = 10\log_{10}\left|\frac{1-{S_{11}}^2}{{S_{21}}^2}\right|, \quad (105)$$

$$SE_R = 10\log_{10}\left|\frac{1}{1-R}\right| = 10\log_{10}\left|\frac{1}{1-{S_{11}}^2}\right|, \quad (106)$$

5 EQUIPMENTS AND SETUPS

5.1 Vector network analyzer

The measurements were done by using two types of VNAs. The first VNA model was Agilent 8510B (Figure 9a) that was used for two-port waveguide measurements. The model had an operating frequency range of 0.045-110 GHz. The second VNA was Hewlett Packard 8720ES (Figure 9b) model which was used for one-port DAK-TL measurements. The VNA had operation frequency range of 50 MHz to 20 GHz. In the waveguide measurements, the VNA setup (Figure 9a) was connected to a waveguide from VNA ports via high-quality cables to the waveguide adapters. In DAK-TL measurements, the VNA that was connected to the DAK-TL one port (left side) was used.

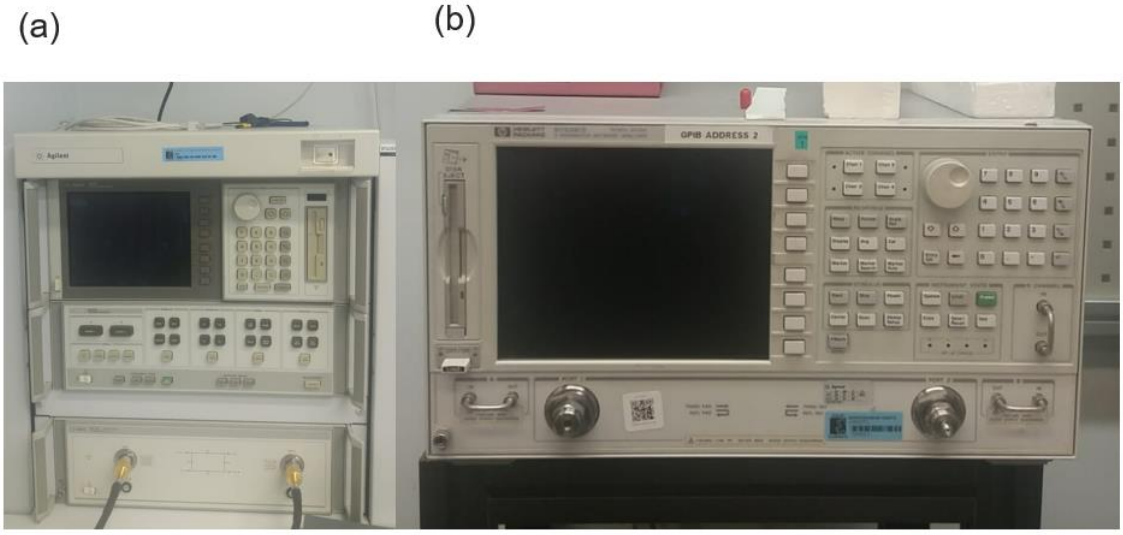

Figure 9. VNAs for measurements: (a) VNA model (Agilent 8517B) is for waveguide and (b) VNA model (HP 8720ES) is for DAK-TL measurements

5.2 The Dielectric Assessment Kit for Thin Layers

DAK-TL is a dielectric assessment kit designed for characterization of dielectric and magnetic properties of the wide range of materials at broad frequency range and high precision. The requirement is that solid materials have a thickness in the range of 0.1-10 mm and liquid materials have quantity of 10–50 ml by volume. DAK-TL is the most suitable for measuring materials that are homogenous and isotropic. [46]

The DAK-TL consists mainly of two parts which are the sample platform and the measurement head (Figure 10) [47]. The upper part of the device is the measurement head that is connected via magnets and screws to the sample platform. DAK-TL is connected to VNA with a coaxial cable and via a USB port to a computer to use the software that controls the calibration and measurement. The sample is placed on the sample platform and the measurement head consists of the probe beam mounter that compresses the sample (controlled

autonomously by software) [47]. When this probe is in a good physical contact with the sample it measures the thickness with precision [46-47]. For the measurements, the calibration was done by following the instructions of the DAK-TL manual.

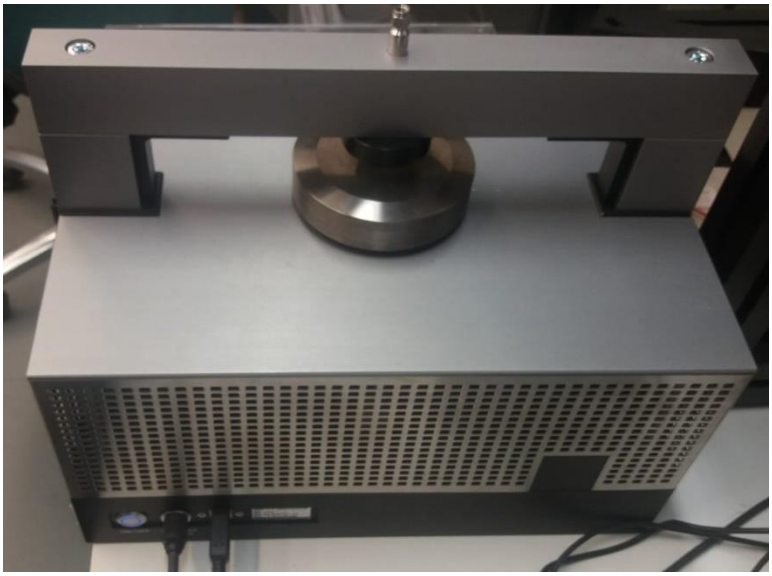

Figure 10. DAK-TL2 dielectric assessment kit which consist of platform and measurement head.

5.3 Waveguide

The waveguide measurements require a manual calibration. The calibration is necessary to avoid errors which can relate to leakages in the system in terms of isolation and directivity. Other errors can exist due to mismatches between a source and a load, and even the frequency response of the whole system.

The manual calibration was done by using Keysight K11644A WR-42 calibration kit. Waveguide calibration was done by measuring short, open and load, transmission and omit isolation. After the calibration, the measurements could be done at the K-band frequency range (18-26.5 GHz) at room temperature (18-22°C). The individual parts in the calibration kit (e.g., alignment pins, shim, short, load) for the rectangular waveguide are shown in Figure 11.

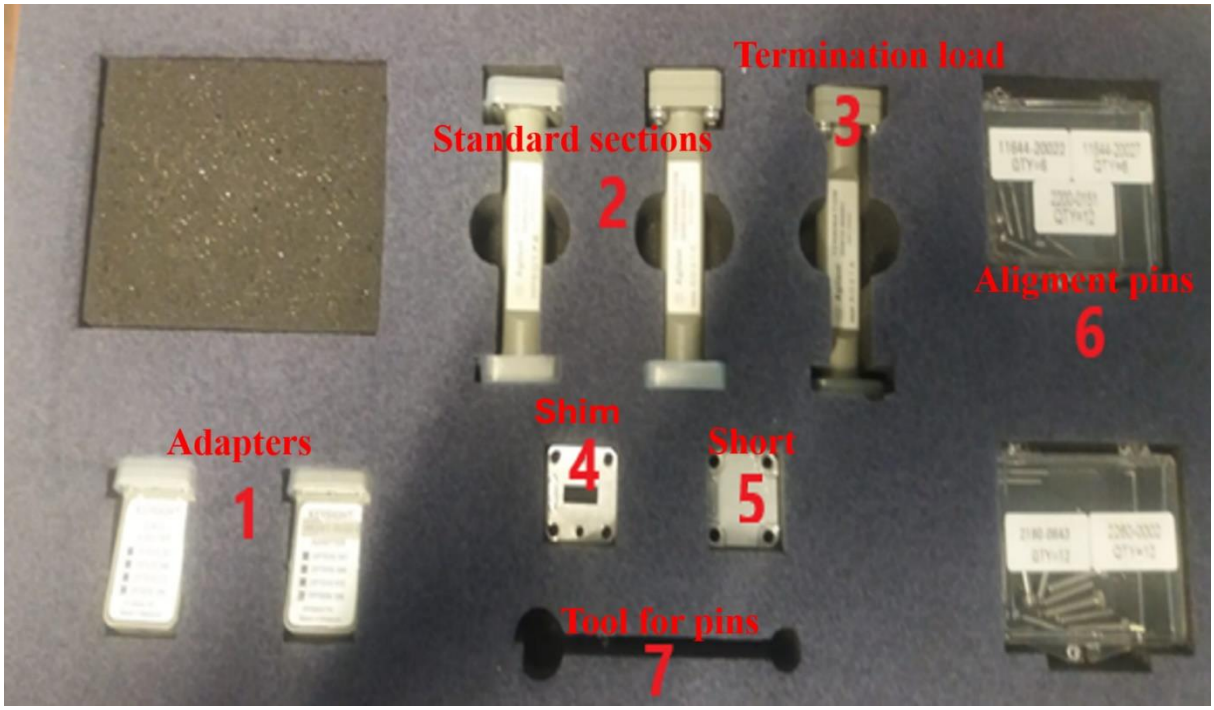

Figure 11. The K11644A WR-42 calibration kit for K-band frequency ranges. All parts related to the calibration can be seen, for example, alignment pins, shim, short, load, and sections.

6 SAMPLES

Seven different absorber structures were made by using different absorber material powders For each sample three absorbing layers was made. Every sample was made by mixing adhesive material with powders and manually tape casting the mixture on a release film through a 1 mm slit. This step was repeated three times for each sample. All the samples were made in room temperature. After the samples hardened, they were cut into 5x5 cm pieces. The preparation of sample mixtures was carried out in the Microelectronics Research Unit. Samples numbers for their structures can be seen in and their thickness for the waveguide and DAK-TL measurements from Table 2 and Figure 12.

Below is the list of all the materials that were used for making this works absorbing samples. List includes materials full name and abbreviate, and from where they were bought or received:

- Sludge of converted gas, (SSAB1) was received from SSAB Raahe factory.
- Combination of blast surface dust and steel smelter, (SSAB2 and SSAB3) were received from SSAB Raahe factory.
- Polyurethane, (Raptorliner) was purchased from K-Rauta.
- Hollow glass microspheres, (HGMS) were received from Kevra Oy.
- Fly ash microspheres, (fillite) were received from Kevra Oy.
- Glass bubbles or hollow glass microspheres iM30k, (3M) were received from 3M^{TM}.
- Carbon nanotubes (Aldrich), (CNT) were purchased from Sigma-Aldrich Inc.

Table 2. The list of the used samples for the measurements and thickness in (mm) during measurement by waveguide and DAK-TL

List of samples:	Used materials:	Sample thickness for waveguide (mm)	Sample thickness for DAK-TL (mm)
Sample 1	CNT+fillite - fillite - fillite	2.15	2.32
Sample 2	CNT+fillite – CNT+fillite - fillite	2.18	0.82
Sample 3	CNT+SSAB1+fillite - fillite	2.11	1.83
Sample 4	CNT+SSAB1+fillite - CNT+Fillite - fillite	2.31	2.58
Sample 5	HGMS - Raptorliner - SSAB2	0,82	1.26
Sample 6	HGMS - Raptorliner - SSAB3	0.96	0.80
Sample 7	3M - RL - SSAB1	0.74	0.50

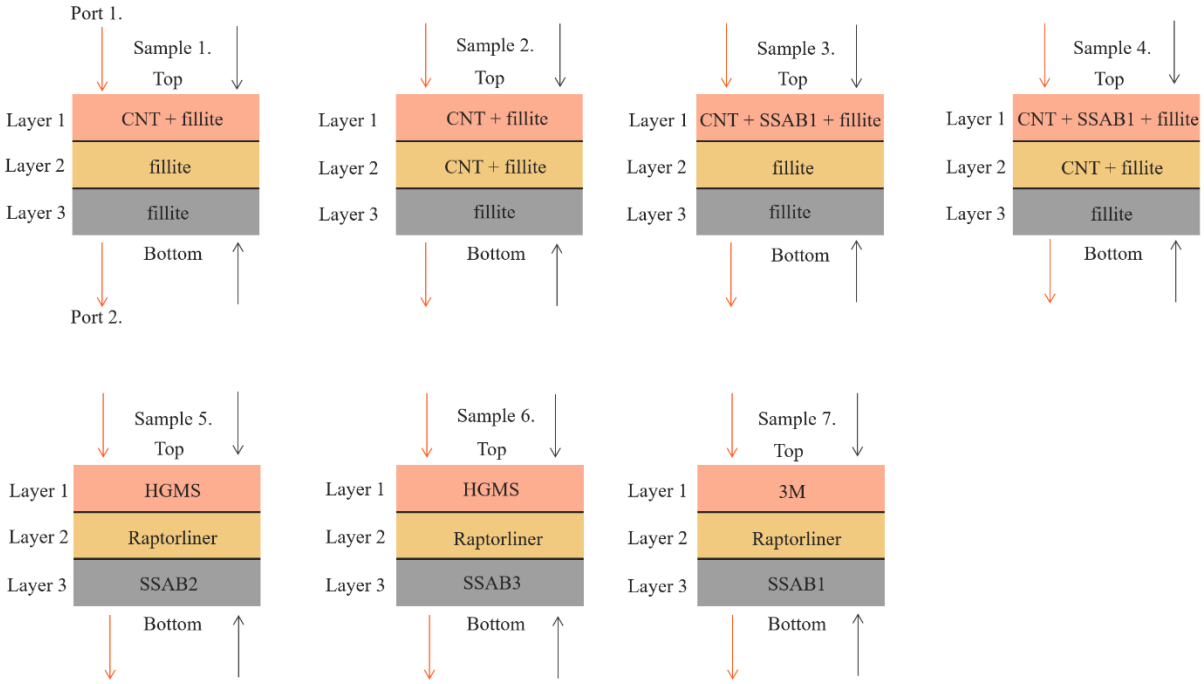

Figure 12. Each sample structures of every layer and composition. The orange arrows represent direction where EM waves for waveguide and grey colour arrows for DAK-TL.

The filler materials were in powder state, whereas the binder material (Raptorliner) was viscous liquid. The powders of HGMS, 3M and fillite were used to add porosity into samples, while CNT and before mentioned Raptorliner would be as absorbing materials. SSABs magnetic powder materials were used in samples as magnetic absorbers.

The HGMS and 3M are both hollow glass microspheres by Kevra and 3M corporations. The spheres in HGMS were 40-60 µm in size compared to 16 µm of 3M, thus making them less pressure resistant. There were used three different SSABs (SSAB1, SSAB2 and SSAB3). Difference in these materials is that SSAB2 and SSAB3 consist of the blast surface dust and steel smelter, while SSAB1 was composed of powder form the sludge of converter gas The consistence of the SSAB masses in iron (Fe) was different. In the SSAB1 there was 66.6% of the Fe, while in SSAB2 was 31.6% and in SSAB3 was 40.2% Fe of the total mass.

35 vol. % of every sample was adhesive material, Raptorliner. While the rest 65% of the sample volume was combination of different filler powders. These filler powders then consisted of 0-25 % carbon (C), 0-25 % magnetic powders and rest 50-75 % was of hollow glass microspheres. As a note to Figure 12 is that in the samples 1-4 it is not written Raptorliner, but it was used as adhesive material and they do consist of 35% as before mentioned, while in samples 5-7 it is mentioned as layer because whole layer is just made of this Raptorliner material.

In all samples the upper layer is the bumpy/rugged and a bit holey, but doesn't have see-through holes, because otherwise sample wouldn't work as absorber. While the lower / downside is smooth due it was backed by release film. The upper and lower side of samples 1-7 are presented on Figure 13.

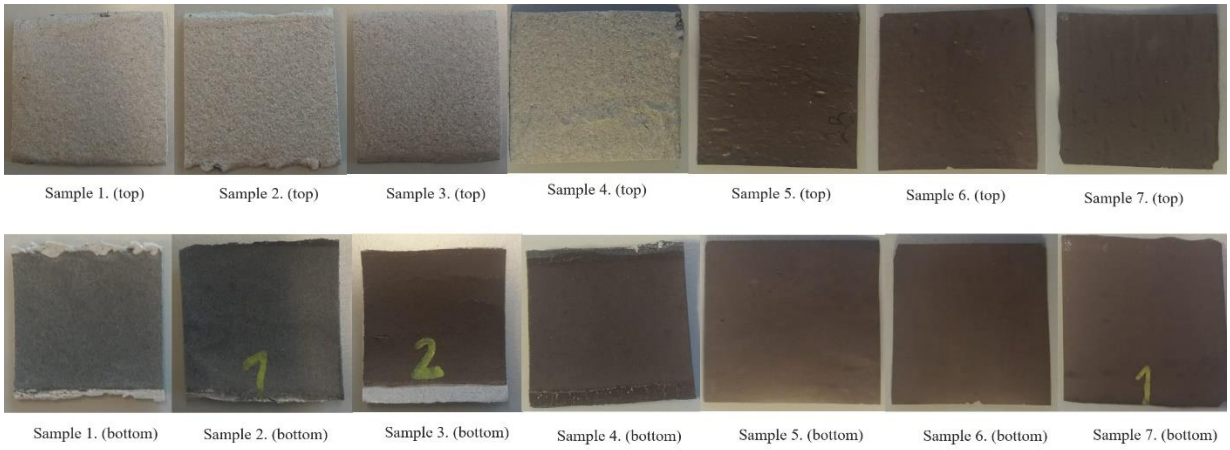

Figure 13. Absorption samples both sides from top and bottom perspective.

7 SIMULATIONS AND MEASUREMENT RESULTS

This section is split into three parts: two first parts are about the waveguide and DAK-TL measurement results, and the third part is a comparison of the measurement results.

7.1 Waveguide measurement results

The shielding effectiveness and reflection loss values were calculated for the multi-layered composite materials based on the calculation theory in previous chapters (the sections 4.2.2. and 4.3.5.). The values were calculated from the measured scattering parameters in a forward (S_{11}, S_{21}) and reverse direction (S_{22}, S_{12}) with a waveguide at the K-band frequency range (18-26.5 GHz).

The shielding effectiveness for reflection (SE_R) in forward direction is shown in Figure 14a. It can be observed that all samples show SE_R values in the range of ≈1-5 dB. Samples 2-3 had the largest SE_R values at the frequency of 18-23.5 GHz. The SE_R values for samples 1, 4-5, and 7 were nearly identical despite frequency increasing. The sample 6 had a slightly more reflection, but the value eventually decreased at 22 GHz to almost the same values as with the samples 1, 5, and 7. Although, the samples 2-3 had a larger SE_R value at the lower frequencies, the magnitude decreased to similar values as with the rest of the samples (approx. 1.5-2 dB).

CNT was added to two layers in sample 2 while CNT/SSAB1 fillers were added to the top layer of sample 3. This resulted the largest SE_R values in the forward direction. It is interesting to note that the sample 4 had a lower SE_R value than the sample 3 even though CNTs were added to the middle layer. The sample 1 had the lowest SE_R value due to absence of fillers in the second and the third layer. As for the samples 5-7, there was not much difference in their multi-layered absorber structures (as shown in the section 2.2, Figure 1b. Thus, SE_R values were not that much different from each other. The sample 6 with HGMS and SSAB3 at the top and bottom layer, respectively, had the largest SE_R value at the lower frequencies. However, at higher frequencies it became the as the same as with samples 5 and 7.

In the reverse direction (Figure 14b), the samples 1-4 had a similar SE_R value in comparison to each other, while the samples 2-3 the smallest SE_R values. In the forward direction the situation was different (Figure 14a). The multi-layered composite structure present in the samples 2-3 can act as a good absorber in the reverse direction. While the structures present in the samples 1 and 4 are better in the forward direction as they reflect smaller amount of the incoming EM waves from the surface. Also, it can be noted that the samples 2-3 had their SE_R values close to 0-0.2 dB at the frequency range of 24-26.5 GHz. The measurements direction change was also visible for samples other samples as the SE_R value difference was considerable due to existing anisotropy of the multi-layered structures.

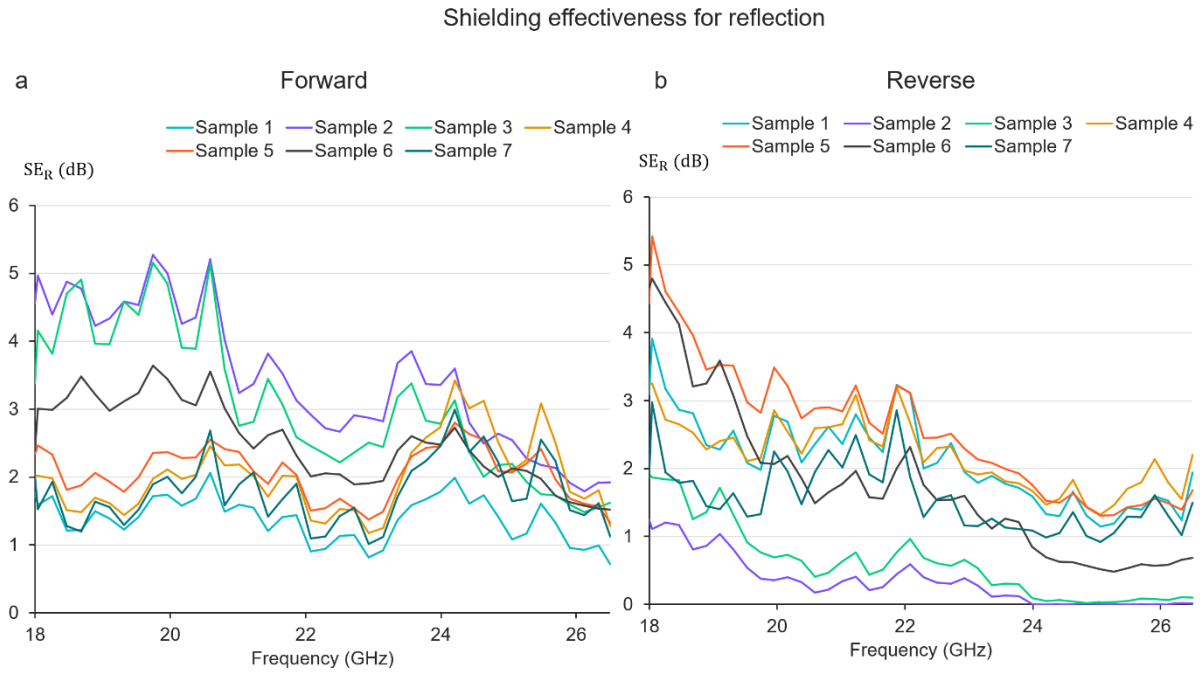

Figure 14. SE_R values measured with a waveguide at the 18-26.5 GHz frequency range for the multi-layered composite materials: (a) for forward and (b) for reverse direction. The measurement direction is shown in the section 6, Figure 12.

The shielding effectiveness for absorption (SE_A) at the frequency range of 18-26.5 GHz in a forward direction is shown in the Figure 15a. It can be seen that for all compositions the SE_A values increase as a function of frequency and were roughly between ≈0-11 dB. The sample 5 had the largest SE_A value at 23.5 GHz. This could be due to the sample 5 having a bottom layer having SSAB2 as a filler. The sample 6 with SSAB3 had a larger attenuation by absorption compared to the sample 5 with SSAB1. Basically, the lower amount of Fe the SSAB filler contains, the larger was the absorption for the composites.

The sample 4 had the largest SE_A value of all the absorbers in forward direction. However, the value started decreases at the frequency of 19.5 GHz, and eventually after a sudden drop at 23.5-24.5 GHz (from 9.85 dB to 5.8 dB) the value stabilized to ≈6-7 dB.

When comparing the samples 1-3, it could be seen that the sample 1 had the largest SE_A value without any added fillers into the top and middle layer, while the samples 2 and 3 had almost identical results that lowered their absorption capabilities due to increased surface reflectivity in the forward direction. From the sample 4 it was seen that SSAB1 filler resulted in better absorption compared to the sample 2 without SSAB1. On the other hand, it also seen that without CNT filler in the middle layer, the SE_A values were smaller (in the sample 3).

Figure 15b shows SE_A values in the reverse direction. It could be seen that while the samples 2-3 had the largest SE_A value in the reverse direction, the situation was totally different for other measurement direction. The sample 2 achieved the largest SE_A value at 24 GHz (up to 28 dB). Between the samples 5-7, the differences in SE_A values very negligible. However, the sample 6 with the lowest Fe concentration in the SSAB filler had a slightly better SE_A value compared to the samples 5 and 7. As for the samples 1 and 4, the results were almost identical in the reverse direction. Even tough, the sample 4 had the largest amount of filler in the individual layers and the sample 1 had the least of the samples 1-4.

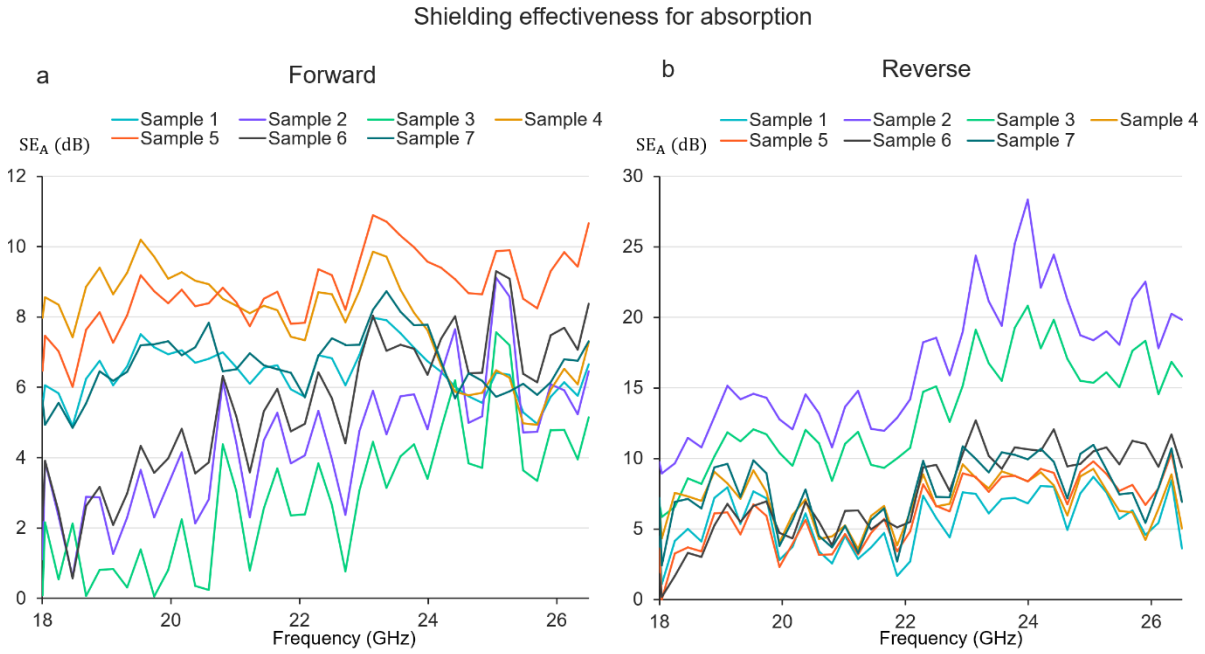

Figure 15. SE_A values measured with a waveguide at the 18-26.5 GHz frequency range for the multi-layered composite materials: (a) for forward and (b) for reverse direction.

Total shielding effectiveness for the samples 1-7 was measured (Figures 16a and 16b). In these measurements, the total shielding effectiveness was just a sum of shielding effectiveness by reflection and absorption. This is because shielding effectiveness for multiple reflections can be neglected on the basis of that explained in the section 4.2.3. From Figure 16a, the sample 3 had the lowest SE_T value, while the sample 5 had the highest value of all samples. It can be observed that for a majority of samples, SE_T values were on around 6-9 dB. Because shielding effectiveness by reflection and absorption fluctuate during the whole measurement (Figures 13a and 14a), this affects the results of SE_T.

In the Figure 15b, the case was totally different in comparison to the Figure 15a. Because the SE_A values for the samples 2-3 were highest in the Figure 13b this resulted for also highest SE_T values. For the sample 2, the value was at 27.5 dB at 24 GHz and for the sample 3 20.5 dB at 24 GHz. The rest of samples were at between 5-10 dB range at 18-26.5 GHz frequency range. The samples 2-3 work well as absorbers in the reverse direction. As for the samples 5-7, the results were alike (Figure 14b) and the same was true for the samples 1 and 4.

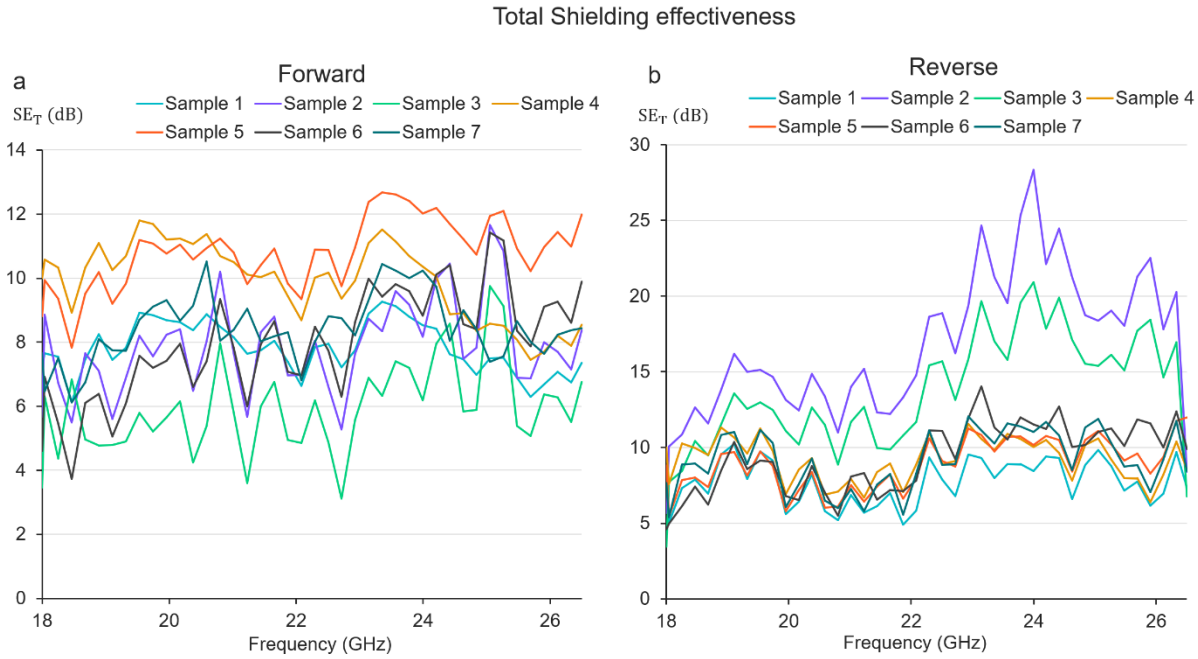

Figure 16. SE$_T$ values measured with a waveguide at the 18-26.5 GHz frequency range for the multi-layered composite materials: (a) for forward and (b) for reverse direction.

The reflection loss (RL) in forward and reverse direction for the samples is shown in Figures 17a and 17b. Once again from all of the samples (Figure 17a), it can be observed that have a quite similar RL and no resonant frequency is present. The sample 1 had the largest RL in comparison to other samples. On the basis of Figure 17a there are two groups of samples (1, 4-5, 7) and (2-3, and 6), which go with an identical pattern. From the frequency of 23.75 to 26.5 GHz, all samples except the sample 7 have almost identical magnitudes of RL.

From the samples 5-7, the samples 6 had the highest RL at the lower frequencies. However, after 23.5 GHz frequency, the magnitude was almost identical with the samples 5 and 7. For the samples 1-4, the sample 1 had the best results. Between the samples 2-4, the sample 4 had the best RL with the CNT in the middle layer and SSAB1 in top layer (at the 18-23.5 GHz range). However, RL started decreasing rapidly after that frequency and then the magnitude was same as for the samples 2-3.

From the samples 2-3 (Figure 17b), it was observed that they had multiple times higher RL compared to other samples. The RL values were91 dB at 24.3 GHz, 85 dB at 25.5 GHz, and 72 dB at 26 GHz. For the sample, a peak value was 45 dB near 25 GHz frequency. By making a direct comparison of Figures 15b and 16b, it can be noticed that when the SE$_R$ was close to 0 dB at higher frequencies, then the magnitude of RL was largest. For the rest samples, the RL were around 3-10 dB.

Figure 17. RL measured with a waveguide at the 18-26.5 GHz frequency range for the multi-layered composite materials: (a) for forward and (b) for reverse direction.

The reflection coefficient (R), transmission coefficient (T), and absorption coefficient (A) were calculated on the basis of the S-parameters for each sample at 19.53 GHz frequency (Figures 18a and 18b). In the Figure 18a, in forward direction, it could be seen that the samples 2-3 had the largest R and T of samples 1-4. The samples 1 and 4 had largest A. The relation between R and T could be also seen in the Figure 17a. At 19.53 GHz frequency, the samples 2-3 had the largest R of the samples 1-4. As for the samples 1 and 4, the largest A resulted into the largest RL (Figure 17a) which was over 10 dB for both samples. As for the samples 5-7, it was seen that the sample 7 had the largest R, which resulted it also having the largest RL of samples 5-7.

While comparing results for the reverse direction, it could be noticed that the samples 2-3 had absorption A were larger than 0.75. This meant that the samples 2-3 did mostly absorb the incoming EM waves, and this could be seen also when considering the results in shown the Figure 15b. . For the samples 1 and 4, the changes for the R, T and A were not that significant as for comparison of the samples 2-3. As for the samples 5-7, it could be observed that the sample 7 had the largest A. Thus, this resulted also into largest RL of the samples (as shown in Figure 17b). However, it was only a marginally larger in comparison to the samples 5-6.

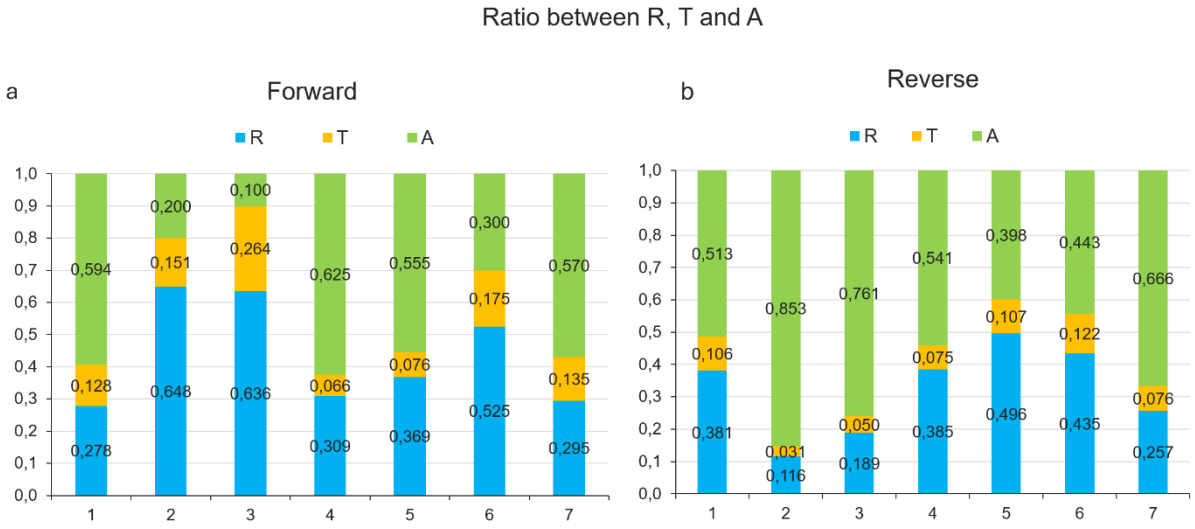

Figure 18. Ratio between R, T and A with waveguide at 18-26.5 GHz frequency for the multi-layered composite materials: (a) for forward and (b) for reverse.

7.2 DAK-TL measurement results

The real and imaginary parts of relative permittivity and permeability, and conductivity were measured with DAK-TL at frequency range of 4-20 GHz. The shielding effectiveness and reflection loss values, and the ratio between the characteristic input impedance and impedance of a free space were calculated on the basis of the calculation theory shown in the sections 2.3.3, 4.1- 4.3.

The SE_R values for the samples 1-7 measured with DAK-TL are shown in the Figure 19. The samples 1, 5, 6, and 7 have the same trend of curvature as the value decreases until 6.5 GHz. After that there was a visible increase of SE_R value up to 15 GHz at which point largest value was achieved for the samples. In the samples 2, 3, and 4, the case was a bit different. From the beginning the value SE_R of the samples began to decreasing around 15 GHz after which the value stabilized. The sample 4 achieve a maximum value of 46 dB. For the samples 5-7, the sample 6 had the best result from the same of kind structures (with a bottom layer made of SSAB3 with 40.2% Fe concentration). Between the samples 1-4, the sample 1 (without any additional CNT and SSAB1 in the middle and bottom layer) had the lowest results of these four samples. While the sample 4 had the largest SE_R value by having SSAB1 added to the top layer and CNT to the middle layer. Between the samples 2-3, the sample 3 had a better result compared to the sample 2. The reason for this could be that the SSAB1 does not improve the absorbance well enough when added to the top layer.

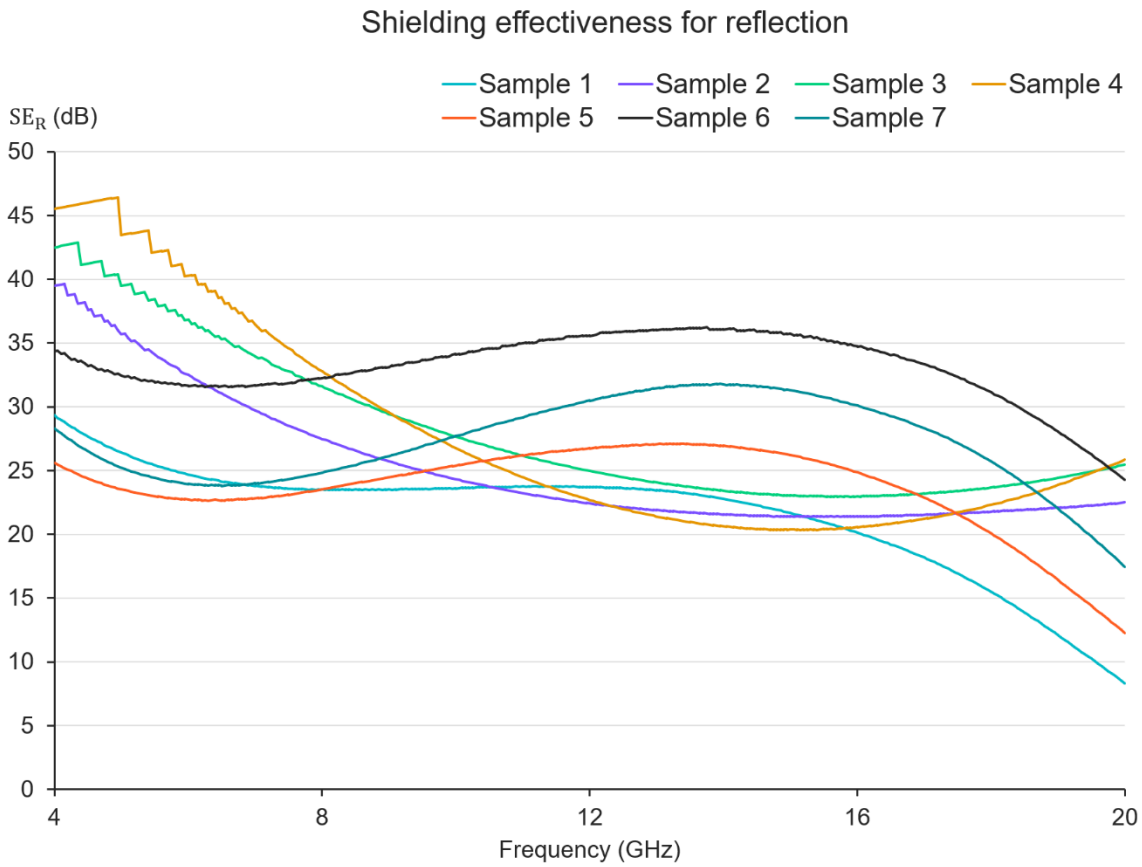

Figure 19. SE_R values measured with DAK-TL at the 4-20 GHz frequency range for the multi-layered composite materials. The measurement direction is shown in the section 6, Figure 12.

Results for SE_A are presented in the Figure 20. The SE_A value does not increase for the samples 5 and 7 until frequency increases to 18 GHz. For the samples 2-4, the SE_A value does increase until the frequency increases to 16 GHz after which theSE_A value stabilizes for samples 2-3. However, for the sample 4, the value starts to have a rapid decline with frequency increasing. As for the samples 1 and 5, their SE_A value starts to rapidly increase after frequency increases to 16 GHz. By careful consideration of the absorber structures, it can be noticed that the sample 1 without additional fillers in the middle or bottom layers has the lowest SE_A value of all the samples 1-4. The samples 2 and 4 with CNT in the top and middle layer have the highest SE_A values. For the sample 4, the RL probably starts to decline due to presence of magnetic SSAB1 filler.

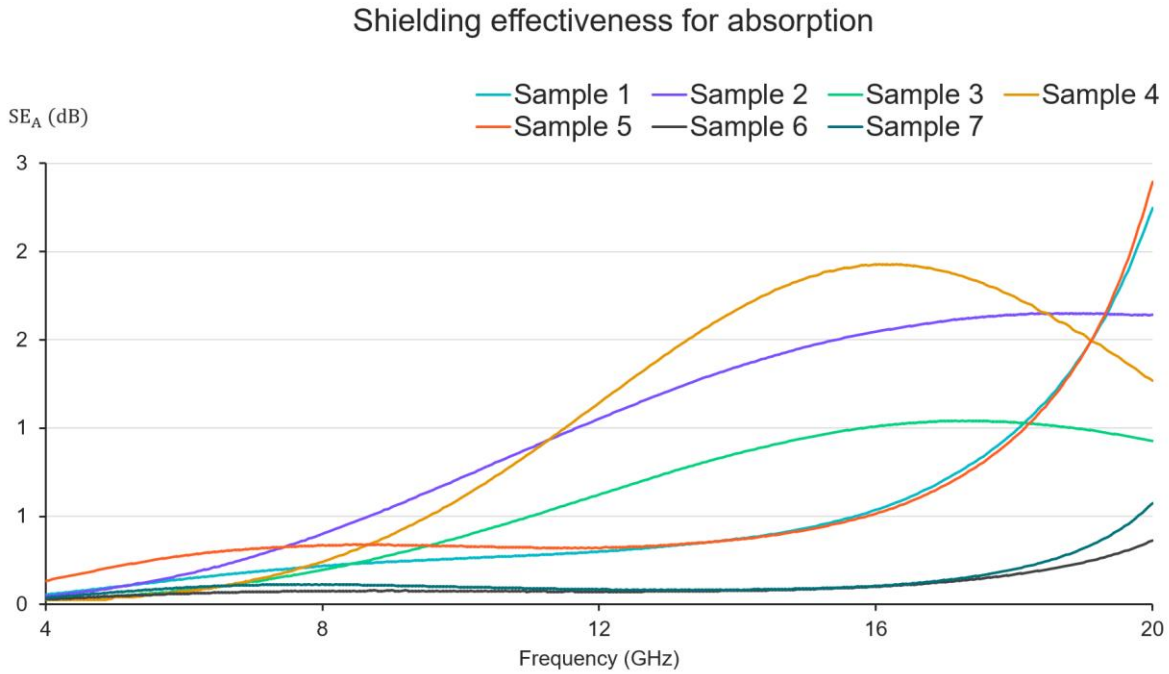

Figure 20. SE_A values measured with DAK-TL at the 4-20 GHz frequency range for the multi-layered composite materials.

In the case of DAK-TL measurements, the SET value was also calculated similar as for the waveguide measurements (sum of SER and SEA). Figure 21 is not similar to Figure 19 close to 20 GHz frequency due to large discrepancies in the SE_R values. To calculate SE_R for DAK-TL was used equation (91) that used relative permeability, frequency at the moment and conductivity. In SE_R equation the smaller conductivity will result into higher SE_R magnitude if the relative permeability is high at same frequency.

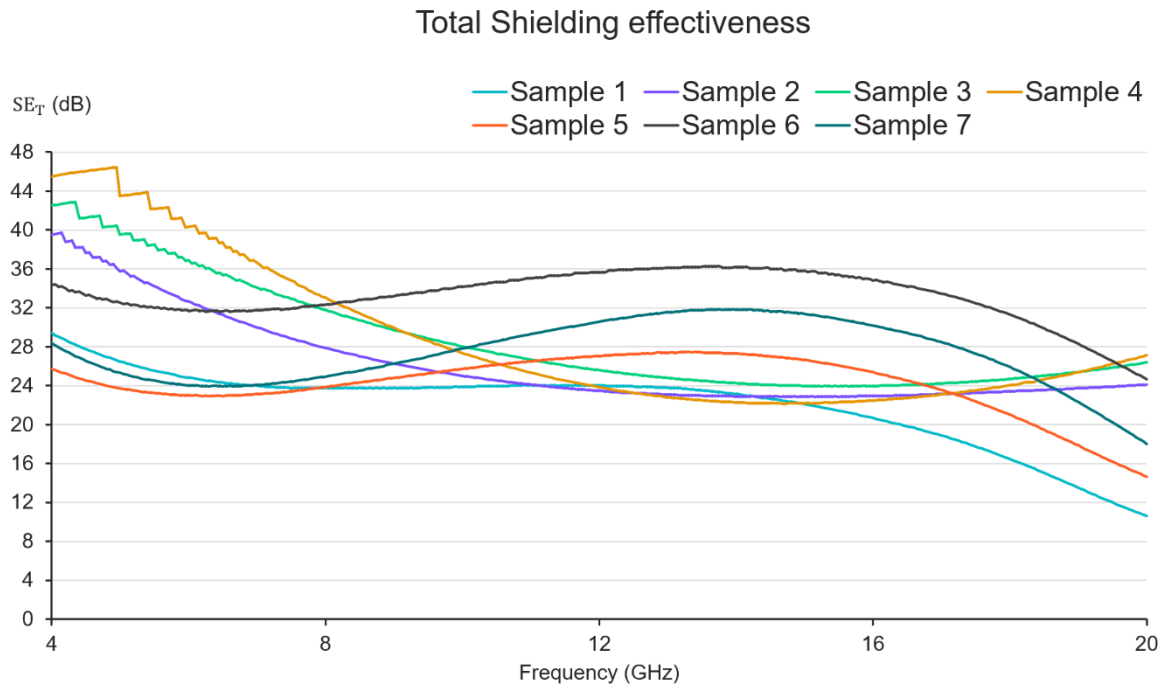

Figure 21. SE_T values measured with DAK-TL at the 4-20 GHz frequency range for the multi-layered composite materials.

By analyzing and plotting data of RL from the DAK-TL measurements, the following Figure 22 was achieved. The resonance frequency for the samples 2 and 4 were at 13 GHz and at 14 GHz with a maximum RL value of 65 dB and 60 dB, respectively. The thickness for the absorbers were 0.82 mm (sample 2) and 2.58 mm (sample 4). The achieved absorption bandwidth for the samples 2 was at frequency range 12-14 GHz, and for sample 3 between range 13-15 GHz. From results the samples 2 and 4 had the largest RL due to existing resonant frequency at X and Y GHz. The samples 1 and 5-7 are below 10 dB for the measurement frequencies (4-20 GHz). Hence, these multi-layered composites do not have an absorption bandwidth.

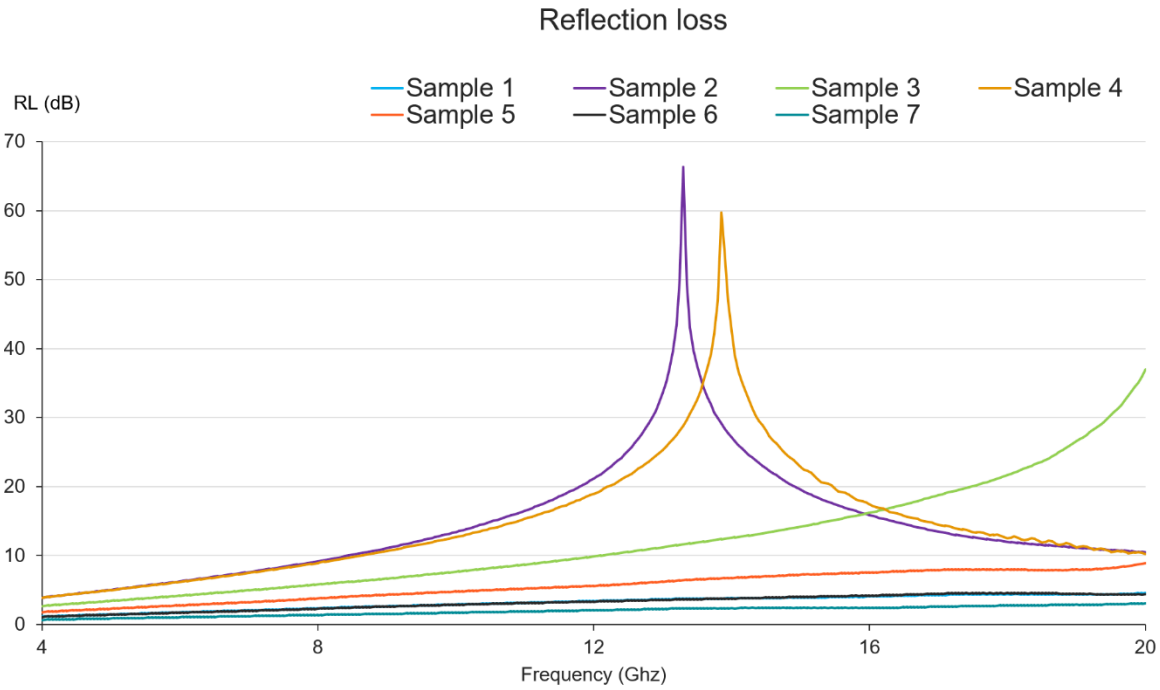

Figure 22. RL measured with DAK-TL at the 4-20 GHz frequency range for the multi-layered composite materials.

The impedance ratio (between η_{in} and η_0) was shown in the Figure 23. By looking at the equations (74-75) at the section 4.2.2 the resonant frequency would occur when the ratio of η_{in} and η_0 would be equal to value of 1. It is clearly visible that the impedance ratio with the samples 2-4 increases with the frequency and is relatively close to value of 1 at the resonant frequency of 13-14 GHz. However, because the impedance ratio still increases with the frequency, the RL values decreases when the frequency increases over the resonant frequency. The sample 3 had a more linear trend at the frequency of 4-20 GHz. On the other hand, the ratio with the samples 1 and 5-7 also increased but it was a very minimal at 4-20 GHz with sample thickness in the range of 0.50-2.32 mm (section 6, Table 2). The sample 7 had the lowest ratio at the frequency range.

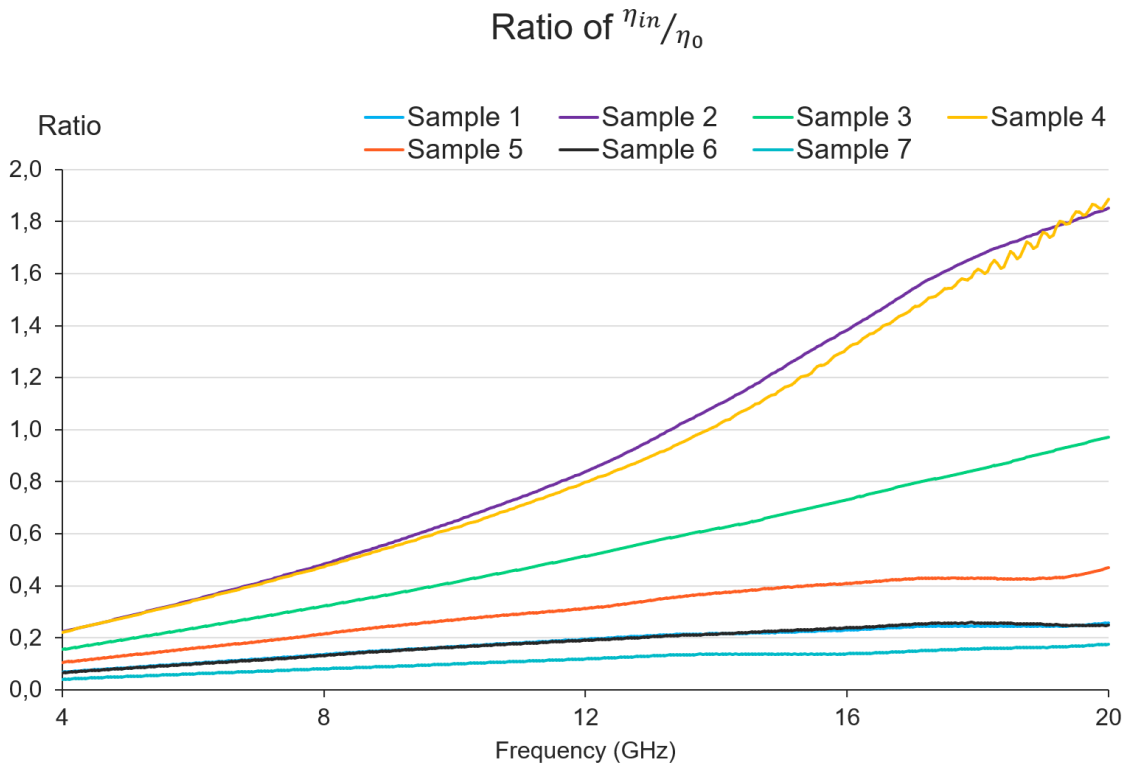

Figure 23. Impedance ratio between the characteristic input impedance and impedance of a free space measured with DAK-TL at the 18-26.5 GHz frequency range for the multi-layered composite materials.

7.3 Comparison of the measured results

From the SE_R values it could be seen that the DAK-TL measured results were a very large in comparison to the waveguide results. It could be seen that in the waveguide results the SE_R values were decreasing as a function of frequency. For the DAK-TL measurements, the samples 1 and 5-7 had a slow increase up to 15 GHz after which they started to decrease. For the samples 2-4, the SE_R values started decreasing rapidly with the increase of frequency from 4 GHz to 13 GHz. For waveguide measurements, SE_R values for both cases were between 0-5.3 dB (at 18-26.5 GHz) while for the DAK-TL measurements the values were in the range of 9-47 dB at 4-20 GHz.

The SE_A values were also different in both measurements. For DAK-TL measurements, all results were on extremely small (≈0.2-2.4 dB at 4-20 GHz). For the waveguide measurements, the values were in the range of 2-10 dB in forward direction and 3-10 dB for samples 1 and 4-7, and 10-25 dB for samples 2-3 in the reverse direction. The attenuation by absorption was multiple times lower in DAK-TL measurements for almost all of the samples in comparison to waveguide measurements.

Because the SE_T value is a sum of the SE_R and SE_A values, it was clear that the total attenuation from the DAK-TL measurements would be considerable better than the waveguide results due multiple times larger SE_R values than SE_A values. The latter were just a small fraction of the total attenuation for the DAK-TL measurements. Although, it is difficult to

compare the SE_T values due to different measurement frequencies, a one thing was clear. The SE_T values were increasing with the frequency for the waveguide measurements, while with DAK-TL measurements the values were decreasing due to significant contribution of SE_R.

The RL was a lot more interesting when the two measurements were compared. It could be seen (in Figure 22) that at higher frequencies the sample 3 seemed to have a resonant frequency above 20 GHz (on the basis of DAK-TL measurements). However, when looking the waveguide measurements (Figure 17a and 17b) there was no resonant frequency present which was a bit strange.The reason for this most likely was due samples not having identical thickness as this can be observed from (section 6, Table 2). For the samples 1-7 (Figure 17a), it could be seen that the RL start to increase at higher frequencies. The RL values at lower frequencies for all the samples without resonant frequency in DAK-TL measurements are below 10 dB at 4-20 GHz and 18-26.5 GHz frequency ranges.

8 DISCUSSION

The waveguide and DAK-TL measurement results at 18-26.5 GHz and 4-20 GHz frequency ranges, respectively, resulted in a wide discrepancy between the calculated attenuation characteristic and properties of the absorbers. Relationship between transmission, reflection and transmission coefficients, and impedance ratio (η_{in}/η_0), shielding effectiveness values in terms of absorption, reflection and total (SE_A, SE_R, SE_T), and reflection loss (RL) generated a lot of information.

For all the measurement results it was noticed that the results of the samples were greatly affected by the frequency as expected. The comparison of the measurements results was cumbersome due to large discrepancies in the magnitudes of the results. However, in overall, the results of the SE_A, SE_R and RL were better for the samples with waveguide measurements. The SE_T values were smaller for waveguide than for DAK-TL due to extremely large SE_R values calculated by using equation (91) with conductivity and relative permeability values.

During the thesis, a lot of work was put into theory and especially into algorithms and calculations. The measured parameters had to be written to a code to calculate the attenuation characteristics for both measurement methods. The calculation for the DAK-TL measurements were more complex in comparison to the waveguide measurements. This meant that errors were more likely to happen in this part of the work if not paying much attention. Overall, most of the factors affecting the measurements had been considered adequately.

For the two-port and one-port measurements, there can be many reasons why the results were so different for the same materials. Because the absorber consisted of three layers and there was a variation in the thickness of individual layers, large discrepancies could be present in the measurement results for the same method (Figure 14 and Table 3).

Samples were initially made into a required size to be measured by DAK-TL. Thus, samples were cut into a smaller size so that they would fit into waveguide shim. Because samples had to be well fitted to the sample holder, the samples had to be sanded very carefully. Another issue with the waveguide measurements is the precise sample size requirement which can have a negative impact on the results if the sample size is not exactly the correct.

In other works, the researchers had done similar measurements for the multi-layered absorbers by using magnetic and dielectric fillers such as carbon black and nanotubes, metals, glass microspheres, polymers, etc. The samples thickness in other works were typically in the range of 1-4 mm, while in this work the thicknesses were 0.8-2.5 mm. By comparing to other works, it was clear that in this work the measurements with DAK-TL and waveguide did not match each other nor results shown in other works. Composites with CNT and magnetic fillers in other works had a resonant frequency at range 2-20 GHz, which was observed DAK-TL at around 13-14 GHz in samples 2 and 4 (Figure 22). The waveguide samples 1-4 had no peaks in forward direction but only at reverse direction for samples 2 and 3, at higher frequency range in comparison to references.

The remaining samples of this work obtained no resonance frequency during measurements. It can be noted that in other works the thicker samples resulted even wider absorption bandwidth, while in this work sample thickness was not optimized. Reason for this is that the objective of this work was the comparison between waveguide and DAK-TL results.

For the future work it could be tried to measure samples with DAK-TL from other side and see how the results would differ. In the future the sample thickness of the best performing samples (2-5) should be adjusted to further improve their absorption properties. Also, it would be interesting if the measurements could be done with other DAK-TL model at higher frequency

range. Due anisotropy present in the absorbers (Figure 15a and 15b), it would be interesting to do more measurements for the best performing samples.

9 SUMMARY AND CONCLUSIONS

The main objective was to characterize the electromagnetic absorbers with two different methods. Multi-layered composite materials were prepared by using polyurethane as matrix, hollow glass and fly ash microspheres, combination of blast furnace and steel smelter dust, and carbon nanotubes as fillers. The measurements were done with two-port waveguide measurement and with one-port dielectric assessment kit at 18-26.5 GHz and 4-20 GHz frequencies. The background on theory of electromagnetic shielding and absorbers was explained in details at the beginning of the work. The attenuation characteristics were calculated on the basis of theory provided in this work.

It was found on the basis of measurement results that DAK-TL and waveguide results did not match in terms of any of the attenuation characteristics (RL, SE_R, SE_A and SE_T). All the samples that were measured with the waveguide performed better compared to the same samples that when measured with the DAK-TL. Even though the SE_A results were not high in either measurement, the results achieved with the waveguide were multiple times better. The SE_R values for the waveguide are a lot smaller in comparison with the DAK-TL samples. Because it is preferable for an absorber that SE_A value is much larger compared to the SE_R values, the SE_T values are a bit misleading (SE_T was many times larger in DAK-TL results than with waveguide).

It can be said that the measurements of the DAK-TL may not be suitable for characterizing absorbers that have anisotropic structures. With DAK-TL it is possible to measure a relative permittivity and a permeability, a conductivity, and a loss tangent. These properties can be measured for the samples that are considered to be relatively homogenous and isotropic. The issue related to the multi-layered absorbers was that the samples were not very homogenous due to the used manufacturing method. Because the multi-layered composites had individual layers with different composition, the properties would be also dependent the measurement direction. The anisotropy was proven by doing measurements of the S11 and S22 to solve reflection coefficient.

10 REFERENCE

[1] Youji Kotsuka, (2019) Electromagnetic Wave Absorbers Detailed Theories and Applications, Josh Wiley Sons, 336 p.

[2] E.F. Knott, J.F. Shaeffer, M.T. Tuley (2004) Radar Cross Section Second Edition, SciTech Pub, 611 p.

[3] Clayton R. Paul (2006) Introduction to Electromagnetic Compatibility, Second Edition, Josh Wiley Sons 1016 p.

[4] Henry W. Ott 12 (2009) Electromagnetic Compatibility Engineering Electromagnetic Compatibility Engineering Henry W. Ott, John Wiley & Sons 880 p.

[5] F. Costa, A. Monorchio, G. Manara. (2016) Theory, design and perspectives of electromagnetic wave absorbers. IEEE Electromagnetic Compatibility Magazine 5.

[6] X. Zeng, C. Zhao, Y. Yin, T. Nie, N. Xie, R. Yu, G.D. (2022) Construction of NiCo2O4 nanosheets-covered Ti3C2Tx MXene heterostructure for remarkable electromagnetic microwave absorption. Carbon N Y 193.

[7] J.D. Baker-Jarvis Michael Janezic John H Grosvenor, J.G. Richard Geyer, J.W. Lyons. (1992) Transmission/Reflection and Short-Circuit Line Methods for Measuring Permittivity and Permeability. IST Technical Note 1355. 120 p.

[8] Yuping Duan Hongtao Guan. (2016) Microwave Absorbing Materials. Taylor Fanrics Group. 402 p.

[9] P. Saville. (2005) Defence R&D Canada-Atlantic DEFENCE DÉFENSE & Review of Radar Absorbing Materials. Defence R&D Canada – Atlantic. 62 p.

[10] Lederer,P. G (1986) An Introduction to Radar Absorbent Materials (RAM). Royal Signals and Radar Establishment Malvern (England). 74 p.

[11] R.L. Fante, M.T. Mccormack. (1988) Reflection Properties of the Salisbury Screen. IEEE Transactions on Antennas and Propagation. Volume: 36, Issue: 10. DOI: 10.1109/8.8632.

[12] J. Fang, T. Liu, Z. Chen, Y. Wang, W. Wei, X. Yue, Z. Jiang. (2016) A wormhole-like porous carbon/magnetic particles composite as an efficient broadband electromagnetic wave absorber. Nanoscale 8(16), 8899–8909.

[13] D. Ding, Y. Wang, X. Li, R. Qiang, P. Xu, W. Chu, X. Han, Y. Du. (2017) Rational design of core-shell Co@C microspheres for high-performance microwave absorption. Carbon Volume 111. 722-732 p.

[14] J.R. Liu, M. Itoh, K.-I. Machida. (2003) GHz Range Absorption Properties Of-Fe/Y 2 O 3 Nanocomposites Prepared by Melt-Spun Technique. Chemistry Letters, Vol. 32, No. 4. 394-396 p.

[15] R. Manna, S.K. Srivastava. (2021) Reduced Graphene Oxide/Fe3O4/Polyaniline Ternary Composites as a Superior Microwave Absorber in the Shielding of Electromagnetic Pollution ASC Omega. 9164-9175 p.

[16] D.C. Jenn. (2005) Radar and Laser Cross Section Engineering Second Edition. American Institute of Aeronautics and Astronautics. 503 p.

[17] Zhao, B., Shao, G., Fan, B., Zhao, W., Xie, Y., & Zhang, R. (2015) Facile preparation and enhanced microwave absorption properties of core–shell composite spheres composited of Ni cores and TiO2 shells. Physical Chemistry Chemical Physics, 17(14), 8802–8810.

[18] M. Qin, L. Zhang, H. Wu. (2022) Dielectric Loss Mechanism in Electromagnetic Wave Absorbing Materials. Advanced Science 9, Issue 10.

[19] Pozar, D.M. (2012) Mircowave Engineering 4th Edition. John Wiley & Sons. 752 p.

[20] (Read 20.2.2022) Skin Depth. Microwaves101. URL: https://www.microwaves101.com/encyclopedias/skin-depth

[21] (Read 20.2.2022) What is skin depth? everythingRF. URL: https://www.everythingrf.com/community/what-is-skin-depth#:~:text=Editorial%20Team%20-%20everything%20RF%20Nov%2029%2C%202017,in%20a%20conductor%20is%20called%20as%20Skin%20Depth.

[22] Laura Hughes. (Read 20.2022) What is Skin Effect in Electrical Engineering? Arrow. URL: https://www.arrow.com/en/research-and-events/articles/the-skinny-on-the-skin-effect

[23] V. Weston (1963) Theory of absorbers in scattering. IEEE Transactions on Antennas and Propagation vol. 11, no. 5, 578-584 p.

[24] Christian Nelson (2016) Calibration methods for material measurements. Master thesis. Department of Electrical and Information Technology, Faculty of Engineering, LTH, Lund University SE-221 00 Lund, Sweden.

[25] Wei-Chih Wang (Read 1.3.2022). Waveguide Theory. URL: http://courses.washington.edu/me557/sensors/waveguide.pdf.

[26] (Read 1.3.2022) What is a waveguide and what are its types? Tutorialpoint. URL: https://www.tutorialspoint.com/what-is-a-waveguide-and-what-are-its-types

[27] (Read 1.3.2022) Microwave Transition Lines, Chapter 1. URL: https://www.cmrcet.ac.in/files/ECE/ececoursefile/19.pdf

[28] M. Irsadi Aksun (Read 1.3.2022) Introduction to Rectangular Waveguides. URL: http://www.ee.bilkent.edu.tr/~microwave/programs/magnetic/rect/info.htm

[29] (Read 1.3.2022) Topic 2, Waveguide and Components. URL https://ombakcomm.files.wordpress.com/2013/06/topic-2-waveguide-and-components-3-ep603.pdf

[30] Akbal, Ayhan & Balik, Hasan. (2006). Fast Rigorous Analysis of Rectangular Waveguides by Optimized 2D-TLM. 3994. 631-637 p.

[31] S. Zva, S. Znb, (2012) Measurement of Dielectric Material Properties Application Note Products. 35 p.

[32] S. Sahin, N. K. Nahar and K. Sertel. (2022) A Simplified Nicolson–Ross–Weir Method for Material Characterization Using Single-Port Measurements. IEEE Transactions on Terahertz Science and Technology, vol.10, 404-410 p.

[33] H. Chen, J. Zhang, Y. Wang, W. Che, Z. Huang, Y. Qiao, J. Luo, Q. Xue. (2022) An Improved NRW Method for Thin Material Characterization Using Dielectric Filled Waveguide and Numerical Compensation. IEEE Transactions on Instrumentation and Measurement, vol. 71, 1-9 p.

[34] A.L. de Paula, M.C. Rezende, J.J. Barroso. (2011) Modified Nicolson-Ross-Weir (NRW) method to retrieve the constitutive parameters of low-loss materials. 2011 SBMO/IEEE MTT-S International Microwave and Optoelectronics Conference (IMOC 2011), 488–492 p.

[35] W. B. Weir, (1974) Automatic measurement of complex dielectric constant and permeability at microwave frequencies. Proceedings of the IEEE, vol. 62, no. 1, 33-36 p.

[36] Lu, B., Huang, H., Dong, X. L., Zhang, X. F., Lei, J. P., Sun, J. P., & Dong, C. (2008) Influence of alloy components on electromagnetic characteristics of core/shell-type Fe–Ni nanoparticles. Journal of Applied Physics 104(11).

[37] Xiang, J., Li, J., Zhang, X., Ye, Q., Xu, J., & Shen, X. (2014) Magnetic carbon nanofibers containing uniformly dispersed Fe/Co/Ni nanoparticles as stable and high-performance electromagnetic wave absorbers. J. Mater. Chem. A, 2(40), 16905–16914 p.

[38] Liu, X. G., Ou, Z. Q., Geng, D. Y., Han, Z., Xie, Z. G., & Zhang, Z. D. (2009) Enhanced natural resonance and attenuation properties in superparamagnetic graphite-coated FeNi3nanocapsules. Journal of Physics D: Applied Physics, 42(15).

[39] Wen, S. L., Liu, Y., Zhao, X. C., Cheng, J. W., & Li, H. (2014) Synthesis, dual-nonlinear magnetic resonance and microwave absorption properties of nanosheet hierarchical cobalt particles. Physical Chemistry Chemical Physics, 16(34) 18333-18340 p.

[40] Yuan, L., Xiangxuan, L., Rong, L., Wu, W., & Xuanjun, W. (2015) Design and fabrication of carbon fiber/carbonyl iron core–shell structure composites as high-performance microwave absorbers. RSC Advances, 5(12), 8713–8720 p.

[41] S. Celozzi, R. Araneo, G. Lovat (2008) Electromagnetic Shielding, John Wiley & Sons. 361 p.

[42] Peng, Mengyue & Qin, Faxiang. (2021) Clarification of basic concepts for electromagnetic interference shielding effectiveness. Journal of Applied Physics. 130. 225108 p.

[43] K. Wyatt, R.J. Jost, (2013) EMC Pocket Guide : Key EMC Facts, Equations and Data, SciTech Publishing Inc. 63 p.

[44] Kim, H. M., Kim, K., Lee, C. Y., Joo, J., Cho, S. J., Yoon, H. S., … Epstein, A. J. (2004) Electrical conductivity and electromagnetic interference shielding of multiwalled carbon nanotube composites containing Fe catalyst. Applied Physics Letters, 84(4), 589–591 p.

[45] Zhang, H.-B., Yan, Q., Zheng, W.-G., He, Z., & Yu, Z.-Z. (2011) Tough Graphene−Polymer Microcellular Foams for Electromagnetic Interference Shielding. ACS Applied Materials & Interfaces, 3(3), 918–924 p.

[46] (Read 26.2.2022) DAK-TL-P Best Practices URL: https://speag.swiss/products/dak/overview/

[47] (Read 26.2.2022) DAK–Dielectric Assessment Kit Product Line URL: https://speag.swiss/assets/downloads/products/dak/free_downloads/AN_DAK-TL_Best%20Practices.pdf